University of Southampton

Thesis submission for Master of Philosophy

Polar Southern Ocean Dynamics from Satellite Altimetry

Author:

Jack Hooley

Faculty of Environmental and Life Sciences

School of Ocean and Earth Science

August, 2018

University of Southampton

Abstract

Faculty of Environmental and Life Sciences
School of Ocean and Earth Science

Master of Philosophy

Polar Southern Ocean Dynamics from Satellite Altimetry

by Jack Hooley

The polar Southern Ocean is a region of complex interactions between the ocean, atmosphere, and cryosphere which have great influence on climatically important processes such as sea ice formation, ice shelf melt, and the production of Antarctic Bottom Water. These processes has been shown to have far-reaching consequences, though the exact nature of their driving mechanisms is not well understood. This is partly due to the inhospitable nature of the region, which makes research voyages difficult, dangerous, and costly; resulting in a sparse distribution of *in situ* measurements restricted to only a few locations. Furthermore, conventional satellite altimetry is incapable of taking measurements in the presence of sea ice, leading to a lack of data in winter months and a bias towards summer. This study aims to address this.

Here, a specially-processed dataset from CryoSat-2 enables measurements of sea surface height to be taken from specular returns from sea ice leads. These are used to provide a picture of polar Southern Ocean dynamics throughout the year. The first objective of this study is to assess the ability of this dataset to capture the seasonal-to-interannual variability of sea surface heightin the polar Southern Ocean. It is shown that the altimetry data has this ability. Comparison with climate indices and *in situ* data reveal that this is a valuable new tool for the investigation of ocean dynamics in the presence of sea ice.

The second objective uses this dataset to analyse the variability and drivers of the Antarctic Slope Front, a frontal system around much of Antarctica's shelf that plays an important role in regulating shelf water properties. Analysis shows that its transport is maximum in April – June and minimal in December – February. This seasonality is near-ubiquitous around the continent, and it is hypothesised it is rapidly propagated around Antarctica along f/H (f is the coriolis paramater, H is the water depth) contours. Wind stress is identified as a major driving mechanism and a composite of wind stress, sea ice concentration, and sea ice drift data is produced. Maximum Covariance Analysis identifies modes of covariance between it and the altimetry and reveals two separate responses to changes in surface stress, each with a different effect on the Southern Ocean. Both of these modes are shown to be important for Southern Ocean dynamics, and could influence climatologically important processes there.

Contents

List of Figures

UNIVERSITY OF Southampton

Research Thesis: Declaration of Authorship

Print name:	

Title of thesis:	

I declare that this thesis and the work presented in it is my own and has been generated by me as the result of my own original research.

I confirm that:

1. This work was done wholly or mainly while in candidature for a research degree at this University;
2. Where any part of this thesis has previously been submitted for a degree or any other qualification at this University or any other institution, this has been clearly stated;
3. Where I have consulted the published work of others, this is always clearly attributed;
4. Where I have quoted from the work of others, the source is always given. With the exception of such quotations, this thesis is entirely my own work;
5. I have acknowledged all main sources of help;
6. Where the thesis is based on work done by myself jointly with others, I have made clear exactly what was done by others and what I have contributed myself;
7. Either none of this work has been published before submission, or parts of this work have been published as: [please list references below]:

Signature:		Date:	

Acknowledgements

I would like to start by thanking my supervisors, Professor Alberto Naveira Garabato, Professor Sheldon Bacon and Dr Michel Tsamados for the support they provided throughout this project. I am especially thankful to Alberto for his near-inexhaustible supply of pep-talks. His mentorship and encouragement has been an inspiration ever since I was his MSci student, and without his open door I would not have completed this piece of work. I am very grateful for the opportunity to join the scientific team on board RRS James Clark Ross to the Weddell Sea and this was a highlight of my career. I must also thank Andy Ridout and Rachel Tilling, whose processing of the initial dataset and consistent support was invaluable in the early days. Thanks also to Dr Simon Boxall, for the innumerable opportunities to show off my teaching skills to students at the university and surrounding schools. Teaching with Ailia Ashworth on the undergraduate field course for 6 years has been another great highlight.

I must also thank Stephen, Nikki, and Delphine for the many long days we spent together in office $2^{2^2} \times 2^{2^2} / 2^{2^2}$, which I think we can all agree has the best room number. Also to Callum, Iain, Zivi, Tanya, *et al* for our frequent escapes to the pub or cinema that made the hard work we were doing that bit more bearable.

Finally, to my family and friends outside of the academic bubble. Thank you for offering valuable advice after listening to my rambles about work, you helped me make some very difficult decisions. Also to the wonderful members of Team Short Shorts, especially Lucy, Daniel and Alun, for taking me on some unforgettable adventures and providing unending hilarity, drinks, and mud.

1 Introduction

1.1 The Polar Southern Ocean

The polar Southern Ocean is the area of the Southern Ocean that lies south of the southern boundary of the Antarctic Circumpolar Current (Figure 1). Surrounding Antarctica, this region contains several dynamical regimes which can be split into the Weddell (60°W – 50°E), Indian (50°E – 160°E), Ross (160°E – 130°W), and Amundsen-Bellingshausen (130°W – 60°W) sectors.

The surface of the polar Southern Ocean is covered in seasonal layer of sea ice which, at its peak, extends out from the coast to a maximum latitude of 60°S around the majority of the continent. The volume and extent of sea ice in this region is a critical part of the global climate system. The seasonal growth/retreat of sea ice directly contributes to Earth's albedo and partially seals off the ocean surface, inhibiting ocean-atmosphere exchange.

Here, the Southern Ocean isopycnals slope upwards towards Antarctica, some of which breach the surface allowing deep ocean water to interact with the atmosphere. As such, this region is especially important for the exchange of energy, dissolved gasses, and other properties between the (deep) ocean, cryosphere, and atmosphere. These properties are transported to the rest of the global ocean by the lower limb of the meridional overturning circulation. Any variations in the composition and export rate of water masses formed here can have far-reaching consequences. Therefore, understanding the seasonal-to-interannual variability of the processes driving such variations in this region is vital for estimating their effects on global climate.

Arguably the most important water mass exported from the polar Southern

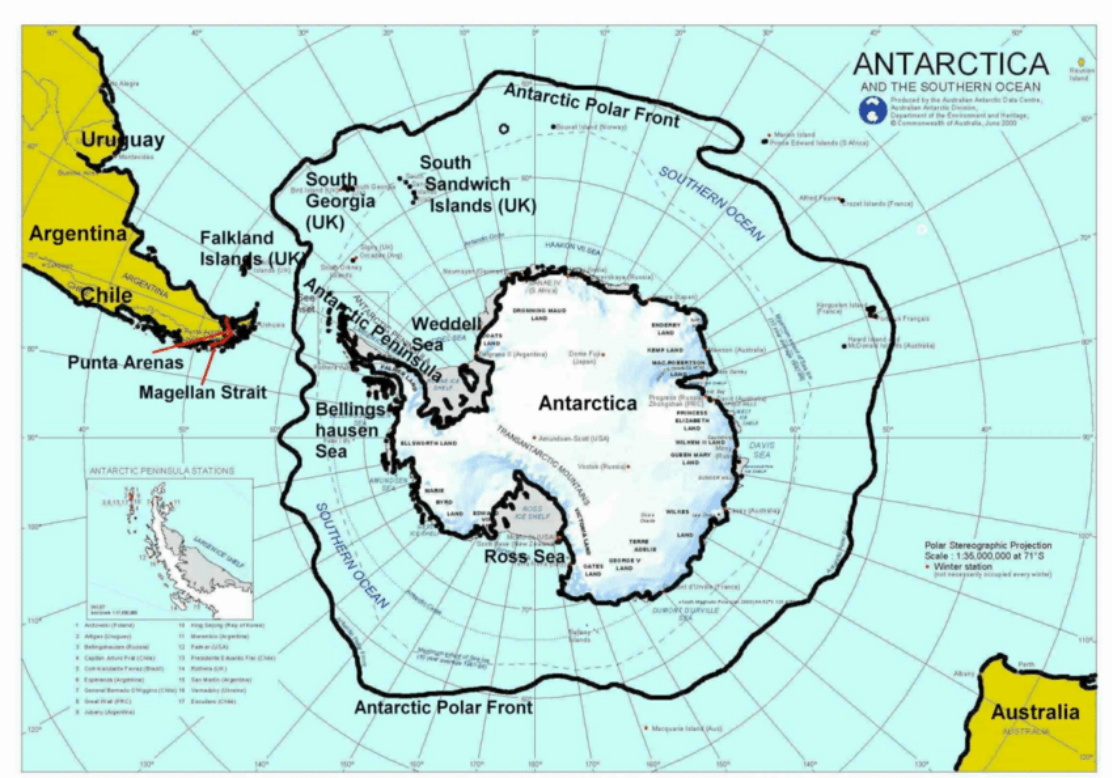

Figure 1: Map of the Southern Ocean. The Southern Ocean is the region of the Southern Ocean that lies south of the Antarctic Polar Front, from `https://www.researchgate.net/Map-of-Antarctica-and-the-Southern-Ocean-From-http-mapperycom-Antarctica-modified_fig1_48227035` [accessed 23 Nov, 2018].

Ocean is Antarctic Bottom Water, as it extends across much of the ocean bottom as the densest water mass in the global ocean (Orsi et al., 1999). Southward North Atlantic Deep Water and other intermediate waters become cooler and more saline due to ocean-atmosphere-cryosphere interactions such as heat exchange with the atmosphere, brine rejection from sea ice formation, and katabatic winds from the Antarctic continent (Jacobs, 2004; Orsi et al., 1999).

The deep Southern Ocean (> 2000 m) has been shown to be warming (due to the ocean uptake of increasing atmospheric heat) and freshening (due to increased freshwater runoff from Antarctica) at a greater rate than the rest of the global ocean (Rhein et al., 2013; Levitus et al., 2012; Rintoul, 2007). As such, it is not surprising that exported Antarctic Bottom Water has also been shown to be warming and freshening in recent decades and its contribution to the global heat budget and sea level rise (due to thermosteric expansion) is significant (Pedro et al., 2016; Purkey and Johnson, 2013, 2010; Böning et al., 2008). Although the processes controlling the rate of Antarctic Bottom Water formation and export are not well understood, investigations into the driving mechanisms do point to processes acting in the seasonally ice-covered regions of the polar Southern Ocean. For example, changes in local wind forcing over the Weddell Gyre has been linked to an intensification of warmer Antarctic Bottom Water exported to the global ocean (Zhang et al., 2016; Meredith and Gordon, 2011).

The Antarctic Slope Front acts as a dynamical barrier between Antarctic shelf waters and the deep offshore environment (Jacobs, 1991). Consequently, it is critical in regulating the exchange of heat, salt and freshwater between the cold shelf waters and warmer subsurface offshore waters. It therefore has great influence on both deep water formation and the melting of ice shelves; cold dense water

masses formed on the continental shelves subsequently form Antarctic Bottom Water after crossing the shelf break (Orsi et al., 1999; Gill, 1973), and warm subsurface waters cross onto the continental shelf and can contribute to ice melt (Hellmer et al., 2012; Smedsrud et al., 2006). However, the seasonal variability of the Antarctic Slope Front is, as yet, not well constrained. This is due to the fact that most studies into the Antarctic Slope Front (reviewed below) are localised to a small region of the Southern Ocean or makes use of data which has too short a period to reliably investigate seasonal variations. It is for these reasons that a study into the variability and drivers of the Antarctic Slope Front system on a circumpolar scale is required to further understand these processes. This study makes use of a novel satellite-derrived dataset of sea surface height in an attempt to quantify the seasonal variability of the Antarctic Slope Front and identify its main driving mechanisms.

1.2 The Antarctic Slope Front System: Variability and Controls

The presence of the Antarctic Slope Front is important for preventing warmer Circumpolar Deep Water from crossing onto the shelf and enhancing ice shelf melt and also regulating the export of Antarctic Bottom Water. Jenkins et al. (2016) present an explanation of the main controlling factors on where the Antarctic Slope Front system is located. In winter, cooling over the ice sheets enhances off-coast katabatic winds which, due to Coriolis deflection, accelerates the easterly winds close to the Antarctic coastline. The resulting Ekman transport from the easterly winds toward the coastline drives downwelling of Antarctic Surface Waters, form-

ing the Antarctic Slope Front which separates the cold, fresh, on-shelf Antarctic surface waters and the warmer, saltier, off-shelf Circumpolar Deep Waters. The presence of the Antarctic Slope Front limits the exchange of on- and off-shelf waters, keeping the shelf waters cold. The stability and effectiveness of the Antarctic Slope Front as a dynamical barrier is driven by a combination of buoyancy forcing on the shelf, to maintain the cold temperatures, and coastal downwelling, to deepen the isopycnals to the sea bed (Jenkins et al., 2016). In regions where the Antarctic Slope Front is weaker, or absent, due to less buoyancy forcing and coastal downwelling, Circumpolar Deep Water can be present on the shelf and has greater potential for ice shelf melt. In these regions, the enhanced ice shelf melt leads to a greater freshwater input, maintaining the absence of the Antarctic Slope Front by preventing buoyancy- and wind-forced deepening of Antarctic Surface Water.

Baines (2009) constructed an idealised model of the Antarctic Slope Front system. This consisted of a water column controlled by quasi-geostrophic dynamics and a downslope flow modelling Antarctic Bottom Water export. The resulting along-slope current is geostrophic and follows f/H contours (f is the Coriolis parameter and H is the water depth) to conserve potential vorticity (Thompson et al., 2014). Using this model, two frontal regimes are found that are dependant on the flux into the down slope plume (Q_0) and the total flux across the shelf (Q_B). The first regime occurs when the downslope flow is dominated by dense water export on the shelf ($Q_0 \approx Q_B$). When this occurs, water on either sides of the continental shelf break sinks in order to enter the downflow. This drives the isopycnals deeper forming the characteristic V-shaped isopycnals of the Antarctic Slope Front. The water properties within the 'V' region are mostly homogeneous, as the sinking sets up unstable stratification which drives mixing. In the model,

the along-shelf flow in this first regime is mostly eastward with downslope flow travelling westwards. The second regime occurs when Q_B is substantially larger than Q_0 so that the water feeding the downflow originates from the shelf only, only the shoreward side of the V forms. In this regime, all along-slope flow is westwards. While this model may capture the controls of the Antarctic Slope Front, it does not fully take into account the role of the easterly winds that form the sea surface height gradient across the continental shelf, instead including it in the combined offshore flux, Q_B. However, this model is "to demonstrate the range of possibilities and the dependence on various parameters, rather than to address any particular situation" (Baines, 2009).

Stewart and Thompson (2013) attempts to connect the theoretical understanding of meridional overturning circulation with the Antarctic Slope Front using Residual Mean Theory. They combined this with an idealised Antarctic continental shelf and results from an eddy-resolving model of the Southern Ocean. As in Jenkins et al. (2016), the Antarctic Slope Front is driven by easterly winds along the Antarctic margins, and forms V-shaped isopycnals. The Antarctic Slope Front arises as a consequence of the eddy-mean balance in Residual Mean Theory, when the continental slope's ability to suppress baroclinic instability is taken into account. The export of Antarctic Bottom Water has been shown to be more sensitive to the Antarctic coastal easterly winds than the midlatitude westerlies (Stewart and Thompson, 2012) , so the focus here is on the sensitivity of the lower branch of the meridional overturning circulation to the coastal easterly winds that drive the Antarctic Slope Front. The V-shaped isopycnals occur in regions of Antarctic Bottom Water formation are a result of suppression of baroclinic instability on the continental shelf. In the model, V-shaped isopycnals can be removed by turning

off the buoyancy forcing on the shelf, producing a very small residual overturning. So, rather than forming V-shaped isopycnals, the colder deeper isopycnals plunge to incrop on the the sea bed, reducing the Antarctic Bottom Water export from the shelf in such regions.

Mathiot et al. (2011) used a range of models each with different resolutions, ranging from coarse (2°) to eddy permitting (0.25°), with the same atmospheric forcing to investigate the seasonal cycle of the westward current associated with the Antarctic Slope Front, the Antarctic Slope Current. Using these models, it was determined that the strength of the coastal easterlies has a strong influence on the water mass transport and seasonality of the Antarctic Slope Current. An increase in the annual mean easterlies by approximately 30% results in a 40% increase in the annual mean Antarctic Slope Current transport. Similarly, increasing the amplitude of the easterly wind seasonal cycle by approximately 30% results in a 30% increase in the amplitude of the Antarctic Slope Current seasonal cycle. Furthermore, if the seasonal cycle was completely removed from the easterly winds, the amplitude of the seasonal cycle in the Antarctic Slope Current transport decreased by more than 50%, while the annual mean transport was unchanged. This shows that that the wind, and its variability, is a major driver of the Antarctic Slope Current variability.

Thompson et al. (2014) used sea glider data across the Antarctic continental shelf break in an attempt to quantify the role of eddies in the cross shelf transport. Focussing on a small region of continental shelf in the Weddell Sea, the glider data showed that, rather than a single velocity core, the westward current associated with the Antarctic Slope Front can have up to three cores separated by approximately 20 km. The driver of the westward current is the coastal easterlies,

which produce an onshore Ekman transport, and a sea surface height gradient which forces a westward geostrophic flow at the shelf break, where it flows along f/H contours for the conservation of potential vorticity. Analysis of the potential vorticity field showed that the vorticity was enhanced at the shelf break, consistent with the V-shaped isopycnals of the Antarctic Slope Front. In the deeper layers, the along-isopycnal thickness gradient also enhanced across the shelf break, which were attributed to balance a suppression of cross shelf transport, which is associated with the Antarctic Slope Front as a dynamical barrier.

Chavanne et al. (2010) used two months of data (January – February, 2009) taken from two hydrographic sections in the southeastern Weddell Sea to identify prominent features along the continental slope. They observed surface and bottom-intensified currents that were in thermal wind balance with the sloping isopycnals across the shelf break. They hypothesised that the undercurrents were caused by the propagation of coastally trapped waves, and that the associated uplift of isopycnals (due to thermal wind balance) allowed warmer deep waters offshore to approach the shelf break. This implies that the existence of the undercurrents may affect the cross shelf exchange by limiting the ability of the Antarctic Slope Front to act as a dynamical barrier between shelf and deep waters. The observed uplift was similar to that caused by seasonal variations in local wind stress, and so it is hypothesised that this mechanism could be comparable to seasonal changes in the Antarctic Slope Front, though the short timescale of this study cannot confirm this.

Núñez-Riboni and Fahrbach (2009) conducted a comprehensive investigation into the driving mechanisms of the current associated with the Antarctic Slope Front using a set of moorings and some ship-based CTD (conductivity, temper-

ature, depth) measurements across the continental slope close to the Fimbul Ice Shelf in the Weddell Sea. Using the relatively long timescale (1996 – 2005), the authors were able to calculate the relative contribution of different forcing mechanisms to the seasonal cycle of the measured current. The mechanisms investigated were Ekman Transport from local wind forcing, thermohaline forcing due to the freshwater input by the ice shelf, and Sverdrup Transport due to the wind curl over the Weddell Gyre. The sea ice concentration is also investigated, as variations in the sea ice throughout the year alters the drag coefficient between the ocean and the atmosphere. The current associated with the Antarctic Slope Front was found to be mostly barotropic (82%), with local wind forcing explaining 58% of the seasonal cycle. Local thermohaline forcing was also important, explaining 30%, while sea ice concentration and Sverdrup Transport were less important, contributing 8% and 4% respectively. While this offers a rather comprehensive insight into the relative dominance of these driving mechanisms, it is based on a single location and so these mechanisms may not have the same dominance ratio in other regions around Antarctica.

Peña-Molino et al. (2016) used an mooring array to directly measure the current associated with the Antarctic Slope Front in the southeast Indian Ocean. Analysis of the profiles showed that the structure of the Antarctic Slope Front current consisted of mainly barotropic (80%) surface- and bottom-intensified jets with a mean transport of -19.2 Sv. The main source of variation in the current occurred in flow below 3000 m, which contributed 80% to the transport variability. The maximum seasonal velocities were observed in autumn (April – June), when the wind stress is also maximum, once again pointing to surface wind stress as a major driver of seasonal variation in the Antarctic Slope Front system.

1.3 Southern Ocean Dynamics: Large-Scale Footprint

Because the Antarctic Slope Front system exists on the edge of the Antarctic continental slope, which lies very close to the Antarctic coastline, the presence of sea ice has meant that only measurements made *in situ* have been able to detect the front, its associated currents, and its seasonal cycle. However, the launch of CryoSat-2 in 2010 has allowed the signature of the Antarctic Slope Front to be detected in the sea surface height measurements within the sea ice region. Kwok and Morison (2015) developed their own algorithm for processing specular radar returns from leads within the sea ice, and used the data to assess the resulting dynamic ocean topography with *in situ* hydrographic measurements, ocean bottom pressure gauges, and satellite-based gravity measurements. The correlations calculated with each indicate strong relationships, supporting the authors claim that CryoSat-2 is a source of dense, high quality data within the ice-covered regions and is ideal for investigation into the circulation changes in these regions.

Following Kwok and Morison (2015), Armitage et al. (2018) used the same data and processing algorithm to investigate seasonal variability in the ice-covered regions of the Southern Ocean. They found that on the Antarctic continental shelf the seasonal cycle in sea surface height was in antiphase with that of the surrounding deep ocean basins; rising to its peak in autumn (April – June). Calculation of geostrophic currents using the dynamic ocean topography (calculated using the CryoSat-2 data and the EGM2008 geoid model (Pavlis et al., 2008)) on the shelf showed the current associated with the Antarctic Slope Front increased during these times, with the calculated flow doubling in autumn. Furthermore, the circulation in the Southern Ocean was shown to be strongly correlated with

the local wind curl, especially within the Weddell and Ross Gyres, and correlations with climate indices such as the SAM and Southern Oscillation Index shows that the data behaves as expected in response to such forcing mechanisms.

Prior to the development of satellite-based Southern Ocean datasets used by the likes of Armitage et al. (2018) and Kwok and Morison (2015), the variability of the large scale circulation in the Polar Southern Ocean was investigated using models. Hughes et al. (1999) made use of data from the Fine Resolution Antarctic Model and Parallel Ocean Climate Model and calculated correlations between the modelled transport through Drake Passage and *in situ* bottom pressure recorders located on the south side of Drake Passage. The large scale transport through Drake Passage was found to be barotropic, and tended to follow f/H contours. High coherence was found between the wind stress on the south side of Drake Passage and the transport fluctuations through it. This lead to the theory that variations in bottom pressure and transport, forced by wind stress, can extend around the continent as they follow f/H contours, which the authors term the 'Southern Mode'.

Hughes et al. (2003) further developed this 'Southern Mode' idea by using a circumpolar array of bottom pressure recorders and tide gauges located on the continental shelf around Antarctica. Using these tools, they were able to investigate the level of coherence around the coastline and on the continental shelf. Calculating coherence between the data from each instrument and modelled transport fluctuations through Drake Passage from the OCCAM general circulation model revealed a circumpolar signal in sea level and bottom pressure that propagated as a barotropic wave and followed f/H contours on timescales up to a year. The Southern Annular Mode (SAM) index had a negative correlation with this sig-

nal, showing how the influence of variations in wind stress can extend around the continent as the 'Southern Mode' propagates.

The 'Southern Mode' is shown to be an important mechanism in the Southern Ocean by studies that investigate the response of the Southern Ocean to variations in forcing mechanisms. For example, Meredith et al. (2004) observed a relationship between transport through Drake Passage and variations in the SAM index. The transport was derived from *in situ* bottom pressure recorders south of Drake Passage and from the OCCAM general circulation model. The coherence of signals around Antarctica allowed by the 'Southern Mode' enables data adjacent to the continent to contain signals about circumpolar transport variability. Meredith and Hogg (2006) used satellite altimetry data in the Southern Ocean and observed a circumpolar increase in eddy kinetic energy 2 – 3 years after an anomalous increase in zonal wind stress. An increase in eddy activity in the Southern Ocean acts to increase the poleward heat flux, which has important consequences for the warming of the Southern Ocean. Zika et al. (2013) investigated the effect of wind variability on the Antarctic Circumpolar Current (ACC) transport. Making use of a series of eddy-permiting ocean-sea ice models they found that, on interannual to decadal timescales, the ACC transport is sensitive to variations in the wind stress located over the path of the ACC (consistent with conventional zonal momentum balance theory) as well as over the coastline of Antarctica (consistent with the coherent 'Southern Mode' theory (Hughes et al., 2003, 1999)). A series of modelling experiments showed that modelled ACC transport variability was due to a linear combination of variations in wind stress along the ACC path and along the Antarctic slope. Furthermore, more realistic forcing experiments showed that the 'Southern Mode' mechanisms dominate the along-ACC path mechanism. Increases

in along-coast forcing results in an increase in ACC transport that is 3 – 5 times stronger than from equivalent forcing along the ACC path. Therefore wind stress along the continental shelf has the potential to affect the Southern Ocean at least up to the northern boundary of the ACC.

1.4 Challenges in Observing the Polar Southern Ocean

The polar Southern Ocean is a difficult place to study. Its strong seasonality and extreme climate makes it impossible for ships to make year-round measurements, leading to an austral summer bias of ship-based *in situ* measurements. This bias can be reduced by deploying moored instruments beneath the surface and under sea ice, however these observations are restricted to local processes and so their effect on the large scale can only be inferred.

Attempts to model this region are also beset by difficulties. Sea ice processes are complex and poorly known and, as such, are parameterised in models. Complex bottom topography makes predicting the formation and transport pathways of deep water masses challenging. Furthermore, conventional satellite altimeters are unable to make measurements of sea surface height in regions where sea ice is present. This has led to a summer bias when making estimations of ocean dynamics from satellite data (for example, Rye et al. (2014)). This project aims to address this shortcoming.

Here, a novel dataset of satellite sea surface height measurements is presented. Altimetry data from the European Space Agency satellite CryoSat-2, processed using a unique algorithm developed at the Centre for Polar Observing and Modelling, University College London, is used to detect sea surface height variations

within the polar Southern Ocean throughout the year. In addition to the usual ice-free data in austral summer, this dataset provides measurements of sea surface topography in winter, when much of the polar Southern Ocean surface is covered in sea ice.

1.5 Aims and Objectives

The aim of this study is to use a novel altimetry dataset and combine it with *in situ* measurements, reanalysis, and other satellite data to analyse the seasonal-to-interannual variability of the polar Southern Ocean circulation and its drivers. This can be split into two main objectives:

1. To assess the ability of the novel altimetry dataset to capture the seasonal-to-interannual variability of the polar Southern Ocean.

2. To analyse and document the variability of the Antarctic Slope Front and assess its dominant driving mechanisms

2 Altimetry and Datasets

Here, an introduction to the datasets used in this thesis is given. First, the CryoSat-2 satellite and the methods of calculating sea surface height in the presence of sea ice using the UCL retracking algorithm are described in Section 2.1. Then the CryoSat-2 dataset itself is introduced in Section 2.3.1, and the choice of geoid model is explained in Section 2.3.2. Finally, in Sections 2.3.3, 2.3.4, and 2.3.5, the datasets used for the validation of the sea surface height measurements and further analysis are described, along with the processing techniques applied to each of them.

2.1 CryoSat-2

The European Space Agency (ESA) satellite, CryoSat-2, is designed to measure variations and long term trends in Earth's cryosphere, and was launched in April 2010 (with data collection beginning in November 2010). It has an orbital period of 369 days, with a 30 day subcycle and its primary instrument is a Synthetic Aperture Interferometric Radar Altimeter (SIRAL) (Wingham et al., 2006).

SIRAL is a Ku-band (13.575 GHz) radar altimeter which operates in three modes: Low Resolution Mode (LRM), Synthetic Aperture Radar (SAR), and SAR Interferometric (SARIn) modes (Wingham et al., 2006). The surface that is being observed (land, ice-free ocean, sea ice, and continental ice sheets) dictates which mode the satellite operates in (Figure 2). In this study, only measurements taken from the ice-free ocean and sea ice regions are analysed.

Over the ice-free ocean, continental ice sheets, and land, LRM is used. SIRAL behaves like a conventional pulse-limited (the size of the pulse footprint is depen-

dent the length of the radar pulse) altimeter. In this mode, the footprint diameter is approximately 1.6 km and the interval between subsequent pulses is approximately 2000 Hz.

Over sea ice, CryoSat-2 switches to SAR mode. Instead of a single radar pulse, the antennae sends out a series of 64 coherent pulses in the fore and aft direction along-track. Exploiting the doppler shift of the return signals from each of these pulses along the fore- and aft-facing parts of the track, the processor can separate the pulses into narrow bands oriented across-track. This reduces the along-track footprint to about 250 m, whilst the across-track footprint is beam-limited (the footprint size is dependant on the width of the beam) and therefore dependant on the satellite altitude (Francis, 2007). Furthermore, the pulse orientation of subsequent bursts means that individual beams overlap, enabling the same point to be measured multiple times by a single satellite pass in a process called 'multi looking'. The separate returns from a particular location can be stacked together to reduce noise (Wingham et al., 2006).

SARIn mode operates in a similar way to SAR, however the return signal received by CryoSat-2 is also picked up by a second antenna, which has a different path length to the emitting antenna. This enables interferometric analysis of the return signals, assisting in reducing errors due to steep across-track slopes. SARIn mode is used for steeply sloping regions, such as ice sheet margins and glaciers. A very small region of the Southern Ocean is measured with SARIn (Figure 2), data in those regions is treated in the same way as SAR.

The boundaries between each satellite mode (Figure 2) are predetermined, with the satellite automatically switching to the relevant mode as it flies over. For static and quasi-static boundaries such as glacier regions and land, these re-

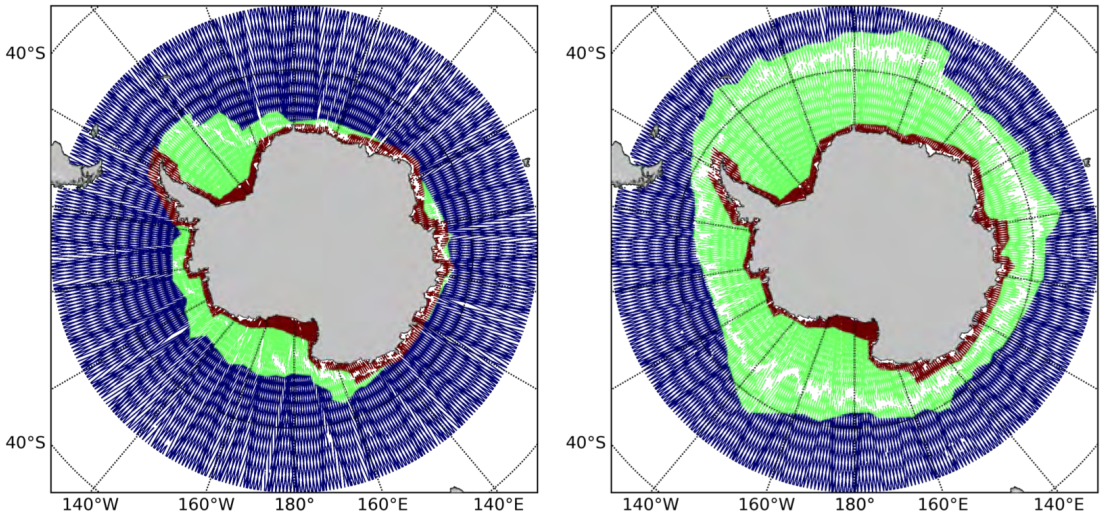

Figure 2: Map of along-track points for September (right) and March (left) 2015. Colours correspond to satellite modes: LRM (blue), SAR (green), and SARIn (red).

main unchanged throughout the year. However, the ocean-sea ice boundary varies monthly due to the seasonal growth and retreat of sea ice. Therefore, to ensure that sea ice is always measured using SAR, the LRM – SAR boundary varies to accommodate the sea ice change. The polygons used in this study describing the mode boundaries are available at: `https://earth.esa.int/web/guest/-/geographical-mode-mask-7107`. The real sea ice edge does not correspond perfectly with the LRM – SAR boundary, and some ice-free ocean is observed using SAR.

2.2 Lead Retracking Algorithm

The data used in this study is ESA's 'Baseline-C' Level-1b CryoSat-2 product, processed to Level-2 at the Centre for Polar Observation and Modelling, University College London (UCL). All geophysical corrections (Table 1) are applied in the

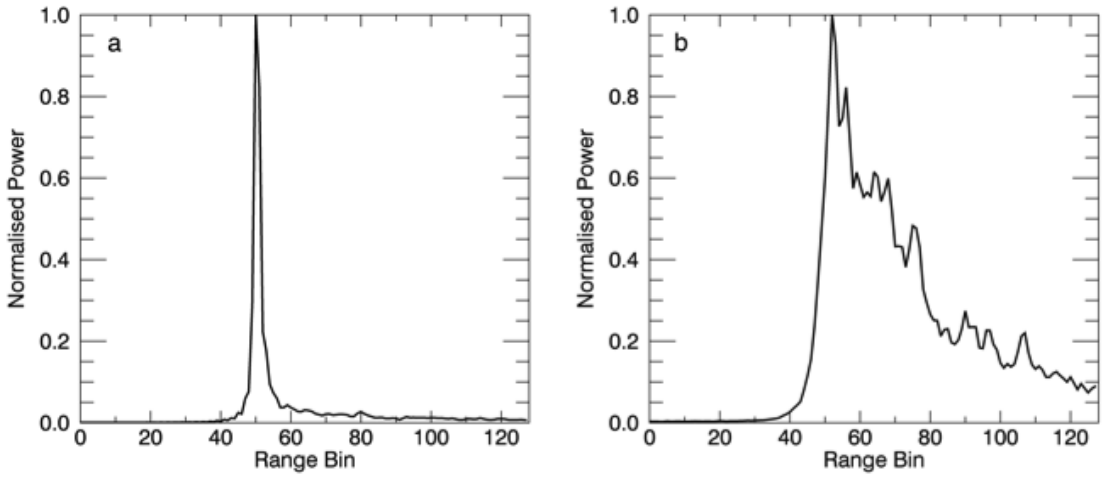

Figure 3: Example waveforms. Specular waveform (left) from sea ice lead regions, and diffuse waveform (right) from ice-free ocean regions. From Tilling et al. (2017).

retracking process, the details of which are available in Bouzinac (2014). Details of the UCL altimeter waveform retracking over sea ice can be found in Tilling et al. (2017), Giles et al. (2012) and Peacock and Laxon (2004), however a brief overview is given here.

Radar echoes from different surfaces differ in their shape, depending on the surface conditions. On one hand the rough surface of the open ocean (due to wind and wave action) scatters the radar pulse, resulting in a diffuse echo waveform (Figure 3, right), with its power on the leading edge rising rapidly, but with a slower tail decay. On the other hand the presence of ice floes in the sea ice region dampen the effects of wind and waves, and so the ocean surface between ice floes is smooth and mirror-like. Hence the echoes are specular in shape (Figure 3, left), with the power of the waveform rising and falling rapidly (Tilling et al., 2017; Peacock and Laxon, 2004). Diffuse waveforms are also obtained from the surface of sea ice floes that surround leads. However, the power return of specular echoes

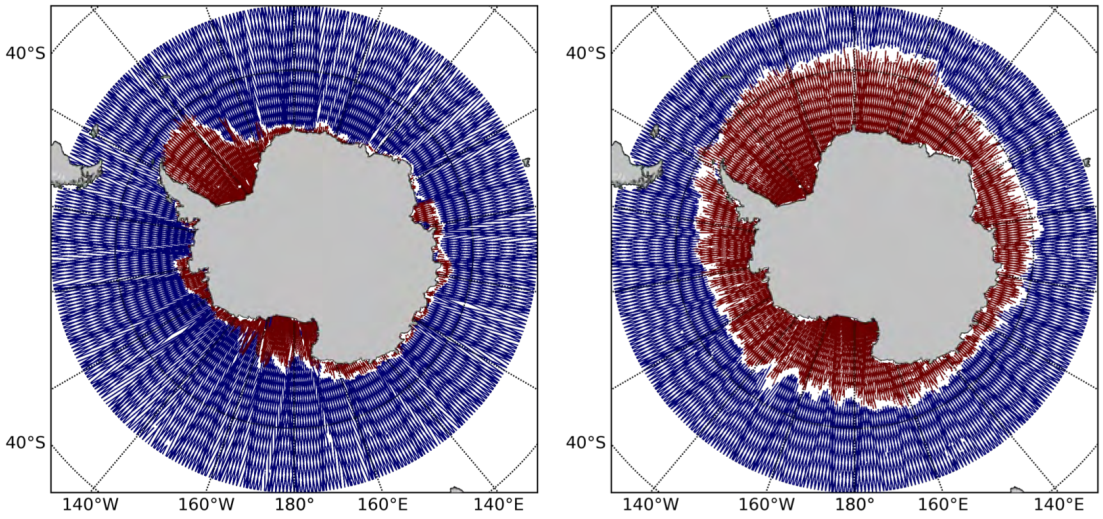

Figure 4: Map of along-track points for September (right) and March (left) 2015. Colours correspond to satellite retracker modes: Leads retracked with the UCL retracker (red), open ocean retracked with a conventional retracker (blue).

compared to diffuse is much greater, meaning that specular returns dominate even if leads comprise only a small percentage of the footprint area (Drinkwater et al., 2004).

Using these two characteristic waveform shapes, it is therefore possible to determine what surface is being detected by calculating the waveform pulse peakiness and then apply the relevant retracker algorithm (Tilling et al., 2017). For specular echoes, the retracking point is located at the maximum amplitude of the function fitted to the waveform, and for diffuse waveforms the retracking point is located where the echo leading edge reaches 70% of the maximum amplitude. For further details on the waveform retracking algorithm, see Tilling et al. (2017).

Correction (all units: m)	min	max	mean	std
Ionosphere	-0.135	-0.001	-0.026	0.017
Dry Troposphere	-2.384	-1.981	-2.254	0.034
Wet Troposphere	-0.304	-0.002	-0.056	0.030
Dynamic Atmosphere (LRM)	-0.337	1.131	0.171	0.139
Inverse Barometer (SAR/SARIn)	-0.651	1.385	0.256	0.127
Ocean Tide	-6.665	6.644	0.000	0.261
Long Tide	-0.070	0.047	-0.005	0.014
Ocean Loading Tide	-0.074	0.088	-0.000	0.013
Solid Earth Tide	-0.146	0.277	-0.005	0.068
Geocentric Polar Tide	-0.016	0.016	-0.000	0.005

Table 1: Information about the geophysical corrections applied to the data in the retracking process. Further details are available in Bouzinac (2014).

2.3 Data

2.3.1 CryoSat-2 Dataset

The Level-2 altimetry data processed at UCL consist of along-track measurements of sea surface height relative to the WGS84 ellipsoid, latitude, longitude, surface type (lead or ice free ocean), and time between January 2011 – December 2016. Also included for each point is the UCL estimation of the mean sea surface, which is calculated from 2 years of CryoSat-2 data (Tilling et al., 2017). Geophysical corrections are applied in the retracking process (Bouzinac, 2014) to account for the fact that the radar pulse passes through Earth's atmosphere, these be sources of significant uncertainty and their details are provided in Table 1. The surface sea ice concentration is also included for each measurement, which is taken from the NASA Goddard Space Flight Center, available at the National Snow and Ice Data Center (Cavalieri et al., 2012).

This is supplied in ASCII files, each containing data from a single satellite

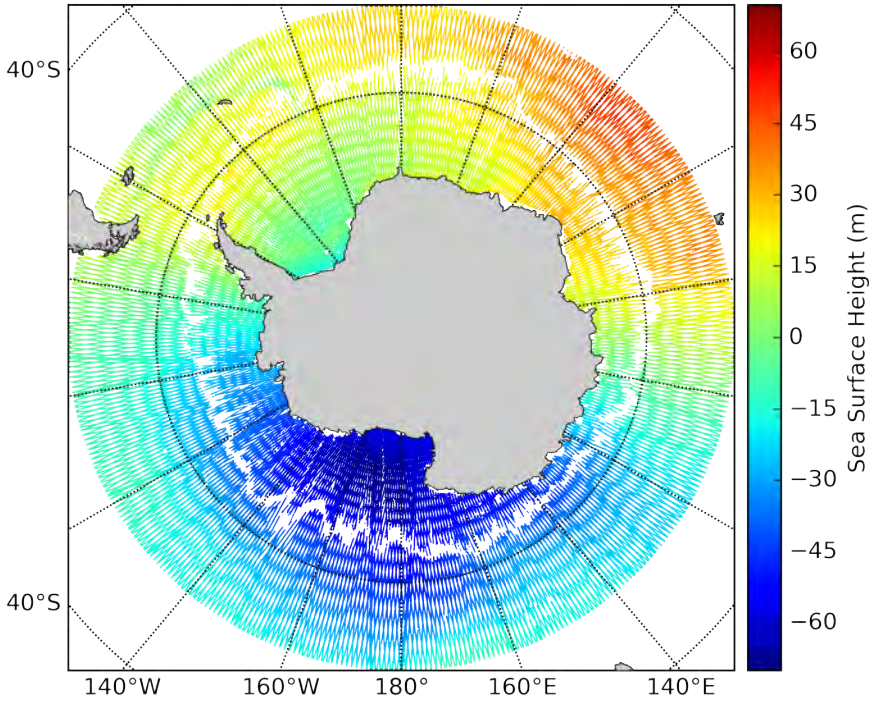

Figure 5: Along-track measurements of Sea Surface Height above WGS84 ellipsoid for September 2015.

pass. On average, there are approximately 430 satellite passes in a month, except for October 2013 where there are only 315. This is due to a power failure on the satellite, which resulted in a loss of data between the 3^{rd} until the 11^{th} October 2013, when the back-up 'redundant' power system was activated (Ridout, personal communication).

A 30 day subcycle means that the whole of the Southern Ocean (and globe) is surveyed in a month, and so the data is split, by months, into satellite passes south of 50°S. For each pass, the satellite flies over the Antarctic continent and therefore the southward (descending) and northward (ascending) tracks observe the Southern Ocean on 'either side' of the continent. Each pass is then separated into its ascending and descending components and processed as two separate tracks.

2.3.2 Geoid Model

With no dynamical processes occurring (currents, wind stress, tide, etc), the ocean surface topography would follow spatial variations in the gravitational field of the Earth. This is the geoid: a surface of equal gravitational potential that follows the topography of the Earth, including oceanic bathymetric features such as mountains, ocean ridges and trenches. Any deviation of the sea surface away from the geoid arises purely due to dynamics and is termed the dynamic ocean topography.

In order to calculate dynamic ocean topography, a geoid model of sufficient resolution is required. Generally, there are two types of geoid model: satellite-only and combined. Satellite-only models use solely satellite-based gravity measurements (for example, GOCE, GRACE), however the resolution is low, due to the high altitude of the satellite. Combined models make use of gravimetry satellites, land- and air-based gravity measurements and, crucially, satellite altimetry

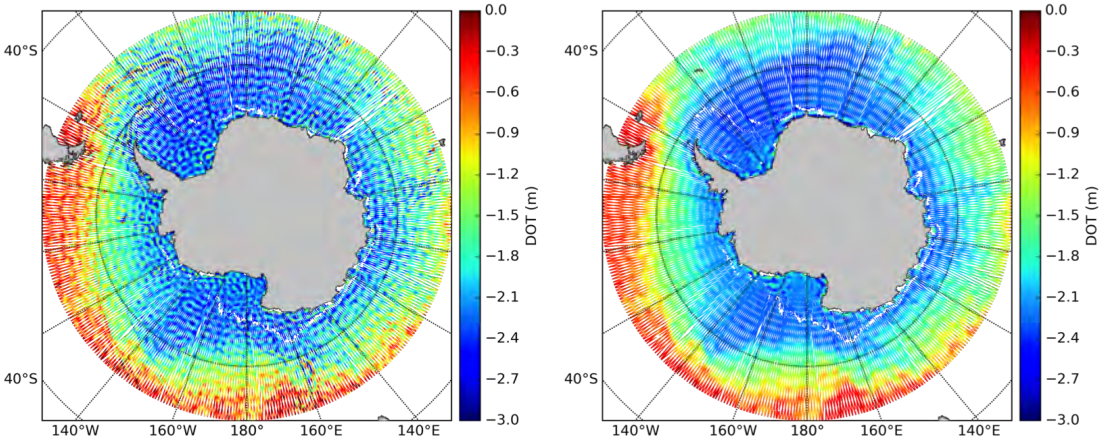

Figure 6: March 2013 dynamic ocean topography calculated using geoid height measurements from the GOCO05s (left) and EIGEN-6c4 (right) geoid models.

to increase the spatial resolution.

Geoid models are provided in spherical harmonics, with a higher degree/order resulting in finer spatial resolution. Generally, satellite-only models go up to degree 300 (the GOCO05s (Mayer-Gürr et al., 2015) model has degree of 280) resulting in a spatial resolution of about 70 km. For combined models, degree can be over 2000 (EIGEN-6c4 (Förste et al., 2014) has order 2190), resulting in a spatial resolution of approximately 10 km. Care must be taken when using combined geoid models, as errors, especially in the altimetry used to construct the geoid, can contaminate the dynamic ocean topography calculated from the geoid and the resulting calculated geostrophic currents.

Whilst the absence of errors derived from altimetry would be an advantage when using a satellite-only geoid model in this study, the low spatial resolution means that such models are inadequate for dealing with the CryoSat-2 dataset in the Southern Ocean. The high resolution altimetry detects short wavelength gravitational features of the Scotia Ridge arc, detectable in the dynamic ocean

topography. The scale of the ridge is below the resolution of the geoid, and are therefore visible in the calculated dynamic ocean topography (Figure 6, left). Its horizontal scale is also similar to that of the dynamic oceanographic features of the region, and so removal by filtering would also remove a substantial amount of oceanographic information. The alternative is to use a higher resolution 'combined' geoid model, EIGEN6c4 (Figure 6, right), which can resolve the gravitational undulations caused by the ridge, resulting in a dynamic ocean topography dataset that is not contaminated by bathymetry-derived geoid features.

However, the use of the 'combined' geoid model EIGEN-6c4 has its own limitations. Figure 6 (right) displays permanent features in the dynamic ocean topography along the Antarctic coastline. Most prominently at 0°W, which occurs in all months and is also visible in other combined geoid models; see Kwok and Morison (2015) for similar features using the EGM2008 geoid model (Pavlis et al., 2008) with CryoSat-2. The permanence of these features, possibly due to errors in the model or land contamination, means that absolute measurement of the dynamic ocean topography and subsequent calculation of dynamics such as geostrophic currents is inadvisable. Variability in these regions, however, is independent of the geoid.

2.3.3 SAM Index

The Southern Annular Mode (SAM) is the primary mode of atmospheric variability in the Southern Hemisphere, consisting of opposing atmospheric pressure anomalies in the mid- and high-latitudes (Marshall, 2003). The SAM index is the difference between zonal atmospheric pressure at 40°S and 65°S. These pressure differences reflect the strength and position of the mid-latitude wind jet. When the SAM

index is positive the westerlies in the mid- and high-latitudes (50°S – 70°S) are stronger than average. A negative index corresponds to weaker than average westerlies. Here, monthly estimates of the SAM index are used for the whole CryoSat-2 period, the data is readily available online (`https://climatedataguide.ucar.edu/climate-data/marshall-southern-annular-mode-sam-index-station-based`) (Marshall, 2003).

2.3.4 Bottom Pressure Recorders

The bottom pressure data used in this study are part of the Permanent Service for Mean Sea Level array across Drake Passage. The bottom pressure recorders used are 'Drake Passage South', which overlaps with the CryoSat-2 period for the first year, and 'Drake Passage South Deep', which overlaps with the CryoSat-2 period for the first 3 years, as only these had data that overlapped with the CryoSat-2 period. The data is available from the PSMSL website (`http://www.psmsl.org`) and is provided in hourly means. The MATLAB tidal harmonic analysis package *t_tide* (`https://www.eoas.ubc.ca/`) is used to extract and remove tidal frequencies with period less than 14 days. Periods longer than this were retained in order to preserve signals with similar periods to that of the altimetry data. After the tidal frequencies were removed, the hourly means were averaged into monthly means (Figure 7). If any gaps existed in the data, the longest gap-free period that overlapped with the CryoSat-2 period was used. Bottom pressure recorders are, by their nature, immune to the inverse barometer effect, and so no steps were made to remove this.

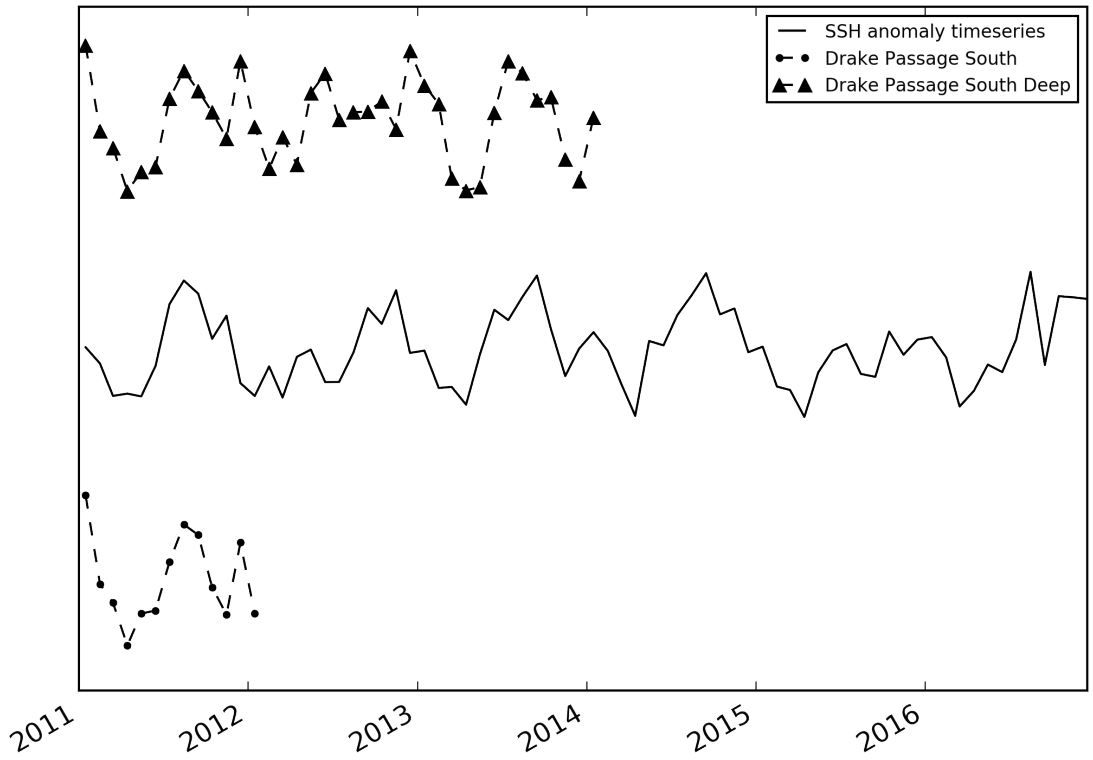

Figure 7: Solid Black Line: Timeseries of the mean sea surface height anomaly for the Southern Ocean (2011 – 2016). Dashed Lines: Timeseries of the bottom pressure data from Drake Passage South (circle markers) and Drake Passage South Deep (triangle markers). This figure is purely to compare the length of each timeseries, so y-axis units are arbitrary and were removed.

2.3.5 Ocean Surface Stress

Wind speed, sea ice concentration, and sea ice drift data were obtained in order to caulculate ocean surface stress and ocean surface stress curl. 10m wind speed data was obtained from European Centre for Medium-Range Weather Forecasts ERA Interim reanalysis (Dee et al., 2011), sea ice concentration data from National Snow and Ice Data Centre (Cavalieri et al., 2012), and sea ice drift data from the Polar Pathfinder Daily 25 km EASE-Grid Sea Ice Motion Vectors Version 3 (Tschudi et al., 2016). The data were restricted to the period January 2011 – December 2015 and then interpolated onto a regular grid (0.5° latitude × 1° longitude).

3 Objective 1: Assessing the ability to capture Polar Southern Ocean variability

Before the dataset of UCL-retracked sea surface height measurements can be used for serious scientific investigations it must first be analysed and processed to ensure that it detects a reasonable level of detail in regards to the dynamic processes in the Polar Southern Ocean. Section 3.1 describes the processing applied to the along-track sea surface height measurements. Section 3.2 describes the methods of calculating and correcting for the offset that occurs along the ocean-ice boundary in the sea surface height data. Sections 3.3 and 3.4 describe calculating the dynamic ocean topography and the methods of gridding the data. Section 3.5 discusses the sources of uncertainty and calculate the error budget from orbital crossover locations. Section 3.6 discusses the validation of the sea surface height data with *in situ* measurements and the Southern Annular Mode Index.

3.1 Along-Track Processing

The UCL lead retracker identifies leads by calculating the pulse peakiness of individual waveforms and the stacked standard deviation of the 'multi-looked' data provided by SIRAL, a pulse peakiness > 18 and stacked standard deviation < 4 is flagged as a lead (Laxon et al., 2013). Specular returns that do not meet these criteria are flagged as 'invalid', and are discarded; this explains why there are some data gaps along the sea ice edge (Figure 5).

Short-wavelength noise and outliers were then filtered out. The sea surface height anomaly is calculated from the sea surface height and the mean sea surface

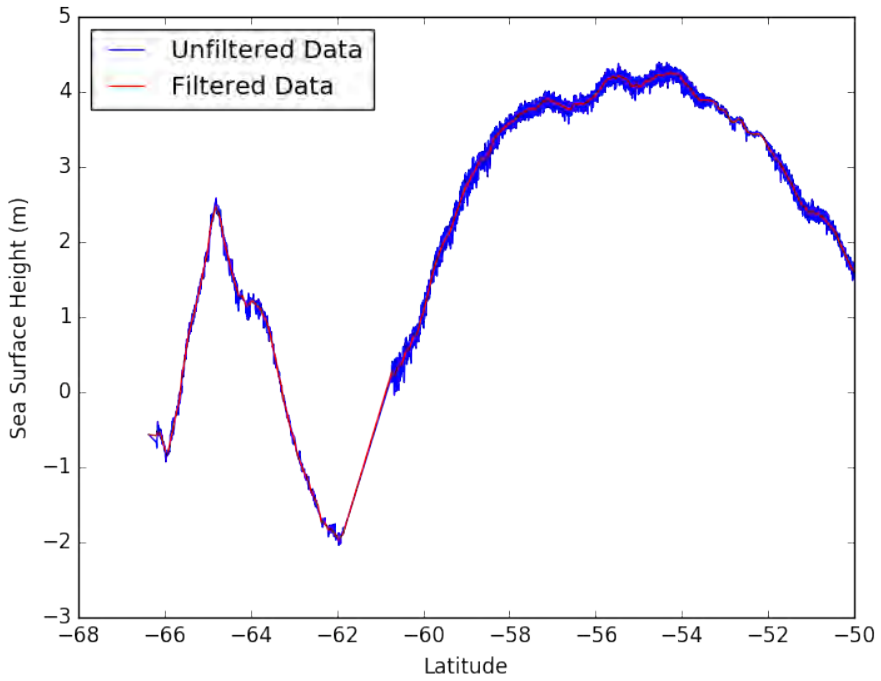

Figure 8: Example unfiltered (blue) and filtered (red) along-track sea surface height. The gap around −61° is caused by the retracking algorithm flagging 'invalid' data at the sea ice edge.

(Section 2.3.1). Any points where the sea surface height anomaly is greater than 0.3 m are discarded. After this, the sea surface height and sea ice concentration data are filtered using a 1-dimensional Gaussian filter (width = 20 km) to remove short wavelength noise (Figure 8).

3.2 Satellite Mode and Retracker Offset

Figure 2 shows the regions that are measured by the three SIRAL modes for two given months (LRM, SAR, SARIn). The LRM – SAR boundary is designed to vary seasonally to match the growth/retreat of the sea ice edge (Section 2.1, Figure 2). In addition to the boundaries between different satellite modes, the

boundary between the ice-free ocean and sea ice lead retracker regions is important (Figure 4). It has been found that differences in data processing techniques (such as satellite mode switches, or retracking algorithms) across these boundaries results in step-like feature in the measurements of sea surface height, here called an 'offset' (Tilling et al., 2017; Armitage et al., 2016; Bulczak et al., 2015). Here, the offset across each boundary is calculated and applied to the relevant dataset. The ice free ocean LRM data is considered the benchmark, and offsets are added to the other datasets to bring them to the LRM 'level'.

The regions of interest are the ice-free ocean measured using LRM, the ice-free ocean measured using SAR (henceforth named $\mathrm{SAR_{ocean}}$), and the sea ice leads measured using SAR/SARIn and retracked using the UCL lead algorithm (henceforth called $\mathrm{SAR_{lead}}$). The boundaries across which offsets are calculated are: LRM – $\mathrm{SAR_{ocean}}$ and $\mathrm{SAR_{ocean}}$ – $\mathrm{SAR_{lead}}$. The offset across the $\mathrm{SAR_{lead}}$ – $\mathrm{SARIn_{lead}}$ boundary is calculated using these same methods but is found to be indistinguishable from instrument noise, as such it is treated as $\mathrm{SAR_{lead}}$.

3.2.1 Decorrelation Scale in the Southern Ocean

The decorrelation scale is the minimum distance between points where, statistically, no significant correlation exists. In the ocean this provides information about the scales of variability, as data inside a given dynamic feature (for example, jets or eddies in the Antarctic Circumpolar Current) should not be correlated with another, separate feature (Bulczak et al., 2015). When estimating the offset, the decorrelation scale is used to dictate the length across a given boundary (half on either side) where data is included in the calculation.

In order to estimate the decorrelation scale for the Southern Ocean, the auto-

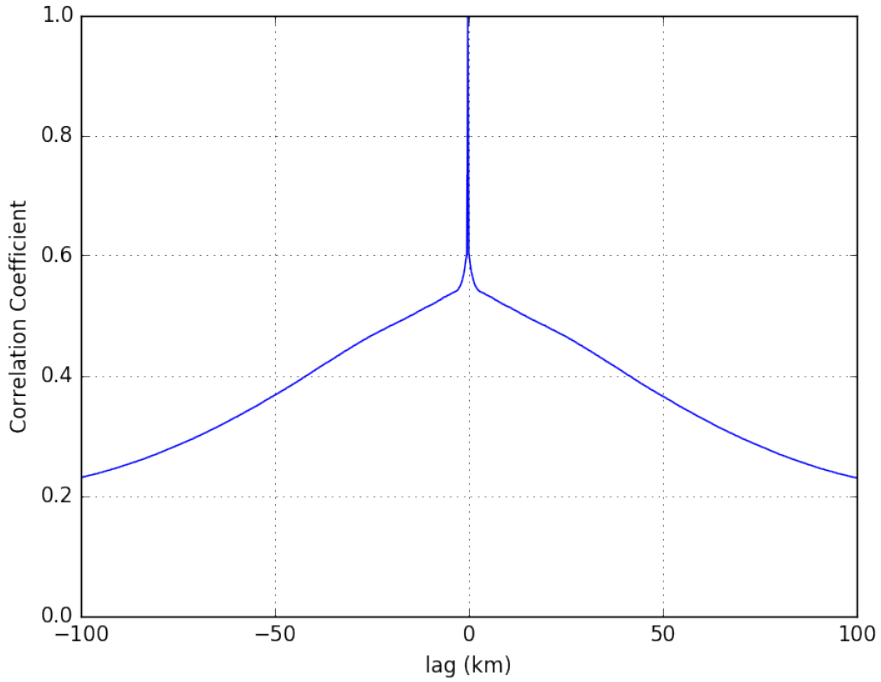

Figure 9: Mean two-sided autocorrelation function for the along-track sea surface height measurements in the ice-free Southern Ocean between January 2011 – December 2016.

correlation function was calculated for each satellite pass (after being separated into ascending and descending ground tracks), using measurements of sea surface height anomaly (taken from the mean sea surface provided by UCL) in the ice-free ocean for each month. Care was taken to ensure that each ground track was sufficiently long (only using tracks with length $> 20°$ latitude) and with minimal data gaps (any tracks with gaps > 5 km are not included). Under these criteria, about 470 satellite passes are used. The autocorrelation results were averaged, providing a mean autocorrelation distribution for the ice free Southern Ocean for the period January 2011 – December 2016 (Figure 9). The mean decorrelation scale is estimated by calculating the distance (lag) when the mean autocorrelation function decays to e^{-1}, in this case, that distance scale is approximately 50 km.

3.2.2 Offset Calculation

Previous work (Tilling et al., 2017; Armitage et al., 2016; Bulczak et al., 2015) calculates the data offset by interpolating the data onto a grid mesh where the grid dimensions are equal to the decorrelation scale. Data within the grid cells that straddles the boundary are used to calculate the offset across that boundary. However, the data inside these cells is acquired over the course of a month, and so the time elapsed between each individual sea surface height data point being measured can be up to 30 days, allowing aliasing errors into the offset calculation. Here, an alternative method for calculating the offset is presented. Rather than gridding the data, the offset in this study is calculated using the along-track data points on a track-by-track basis. This minimises the time elapsed between data points used in each individual offset calculation, reducing the potential for aliasing errors and allows the offset to be analysed on time scales shorter than a month.

The offset across the boundaries (LRM – $\mathrm{SAR_{ocean}}$ and $\mathrm{SAR_{ocean}}$ – $\mathrm{SAR_{lead}}$, shown in Figure 2) is calculated using the along-track measurements of sea surface height data provided by UCL. This data is split into ascending and descending portions of every satellite pass for the complete years of the dataset (2011 – 2015). For each track, the boundary location is defined and all satellite points within half the decorrelation scale (25 km) on either side are extracted to form a 'boundary section', spanning 50 km with the boundary in the middle. Each boundary section is inspected to ensure that all points correspond to the correct surface (all 'ice-free ocean' for the LRM – $\mathrm{SAR_{ocean}}$ boundary, and all 'ice-free ocean'/'lead' on the $\mathrm{SAR_{ocean}}$/$\mathrm{SAR_{lead}}$ sides of the $\mathrm{SAR_{ocean}}$ – $\mathrm{SAR_{lead}}$ boundary) and that there are no data gaps greater than 5 km wide. If both these criteria are met, then the following steps are taken to calculate the offset for that ground track:

$$\mathrm{Offset_{SAR_{ocean}}} = \overline{\mathrm{SSHA_{LRM}}} - \overline{\mathrm{SSHA_{SAR_{ocean}}}} \tag{1}$$

across the LRM – $\mathrm{SAR_{ocean}}$ boundary, and

$$\mathrm{Offset_{SAR_{lead}}} = \overline{\mathrm{SSHA_{SAR_{ocean}} + Offset_{SAR_{ocean}}}} - \overline{\mathrm{SSHA_{SAR_{lead}}}} \tag{2}$$

across the $\mathrm{SAR_{ocean}}$ – $\mathrm{SAR_{lead}}$ boundary. Where $\mathrm{Offset_{SAR_{ocean}}}$ and $\mathrm{Offset_{SAR_{lead}}}$ are the offsets for the $\mathrm{SAR_{ocean}}$ and $\mathrm{SAR_{lead}}$ regions respectively. $\overline{\mathrm{SSHA_{LRM}}}$, $\overline{\mathrm{SSHA_{SAR_{ocean}}}}$, and $\overline{\mathrm{SSHA_{SAR_{lead}}}}$ are the average sea surface height anomalies on the LRM, $\mathrm{SAR_{ocean}}$, and $\mathrm{SAR_{lead}}$ sides of the boundaries, respectively. The data on the $\mathrm{SAR_{ocean}}$ side of the $\mathrm{SAR_{ocean}}$ – $\mathrm{SAR_{lead}}$ boundary are corrected with $\mathrm{Offset_{SAR_{ocean}}}$ before $\mathrm{Offset_{SAR_{lead}}}$ is calculated, this ensures that both offsets are calculated rel-

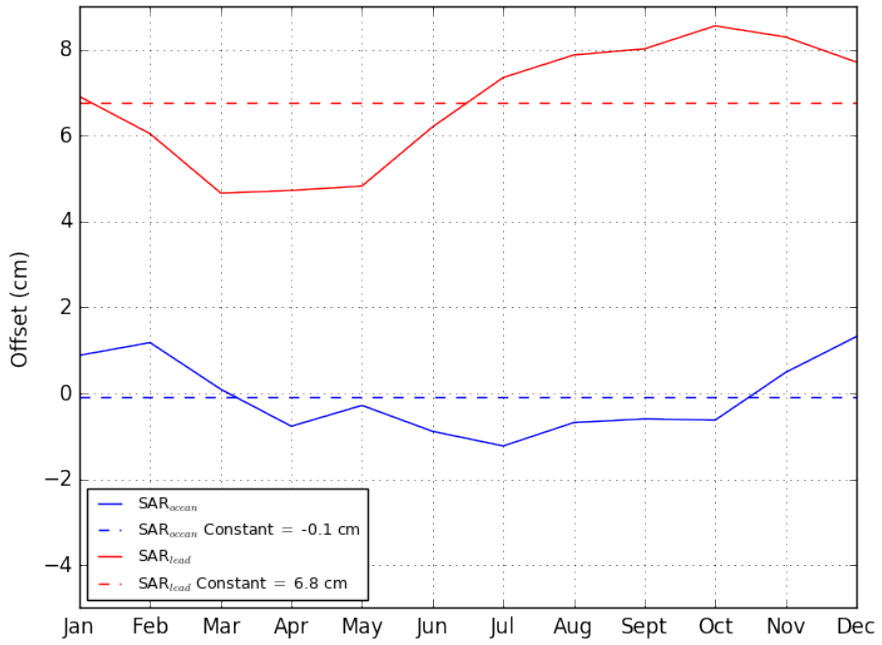

Figure 10: Monthly average offset. LRM – $\mathrm{SAR}_{\mathrm{ocean}}$ (blue) and $\mathrm{SAR}_{\mathrm{ocean}}$ – $\mathrm{SAR}_{\mathrm{lead}}$ (red).

ative to the LRM 'baseline'.

The average offset across each boundary, for every satellite pass, is taken for each month, and all individual months (Januarys, Februarys, etc) are averaged to produce a seasonally varying offset (Figure 10). The mean seasonal offset is also calculated, here called the 'constant offset', which has values of

$$\mathrm{Offset}_{\mathrm{SAR}_{\mathrm{ocean}}} = -0.1 \text{ cm} \tag{3}$$

and

$$\mathrm{Offset}_{\mathrm{SAR}_{\mathrm{lead}}} = 6.8 \text{ cm} \tag{4}$$

Armitage et al. (2016) hypothesised the formation of melt ponds on the surface of ice floes and formation of new ice in the growth season as the reason for the seasonally varying $SAR_{ocean} - SAR_{lead}$ offset. These features would cause 'lead-like' specular returns and therefore bias the sea surface height high.

The offsets are applied to all data, where relevant ($Offset_{SAR_{ocean}}$ is added to all SAR_{ocean} points, and $Offset_{SAR_{lead}}$ is added to all SAR_{lead} points). Two separate altimetry datasets are produced, one with the seasonally varying offset applied and one with the constant offset applied. The validity of these two offset methods and their improvements to the altimetry dataset are tested in Section 3.6.

3.3 Dynamic Topography Calculation

A 0.1° resolution geoid height grid is generated from the EIGEN-6c4 combined geoid model (Förste et al., 2014). The latitude/longitude from the along-track data is used to calculate interpolated geoid height estimations at each individual point. Then the calculation for the dynamic ocean topography (DOT) is simply,

$$DOT = H_{ssh} - H_{geoid} \tag{5}$$

at each point. Where H_{ssh} is the sea surface height above WGS84 measured by CryoSat-2 and H_{geoid} is the geoid height above WGS84 from the EIGEN-6c4 geoid model (Figure 6, right).

3.4 Gridding and MDT Calculation

To enable month-to-month comparison, time series analysis, and use with other datasets, the along-track data are gridded onto a regular grid. The size of the

grid boxes is chosen to maintain as high resolution as possible while reducing the number of empty cells; the along-track resolution can be as fine as 0.25 km but the distance between individual tracks can vary due to the orbital path of the satellite. Therefore the meridional cell length can be shorter than the zonal. The chosen grid resolution is 0.5° latitude × 1° longitude. All along-track points that fall within the grid cell are averaged, if no points fall within the cell then the cell value is left blank (for example, along the sea ice edge).

Figure 11 shows an example of the number of along-track data points used in each cell during the gridding process. The number of data points per cell in the open ocean ranges upward from about 300, while cells within the sea ice zone have between 100 – 300 data points. This is because lead distribution is not ubiquitous throughout the sea ice and so data coverage is more sparse than that of the open ocean.

After gridding, a 2-dimensional Gaussian filter with width = 500 km ($\sigma = 100$ km) is applied (Figure 12). All monthly gridded dynamic ocean topography products are averaged together to produce a representation of the mean dynamic topography (MDT) for the period January 2011 – December 2016 (Figure 12, right). This mean ocean topography can be subtracted from each individual month to produce an anomaly.

3.5 Uncertainty in Sea Surface Height Estimates

The Root Mean Squared (RMS) difference in sea surface height measurements at orbital crossover locations are used to estimate the mean uncertainty for the dataset (Peacock and Laxon, 2004). This method takes into account all the uncer-

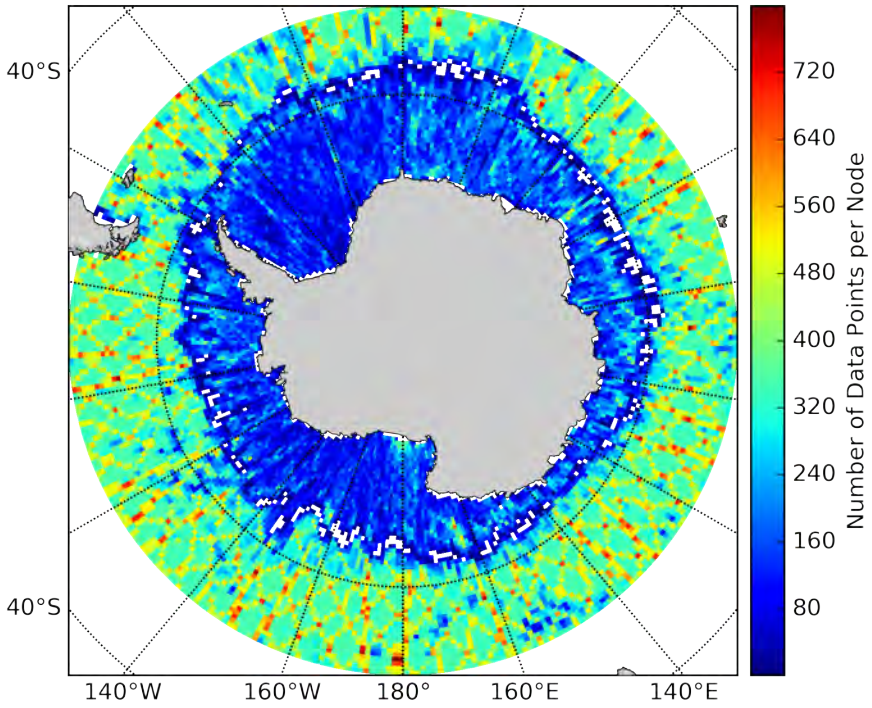

Figure 11: Number of data points included in the gridding algorithm per grid cell for September 2015.

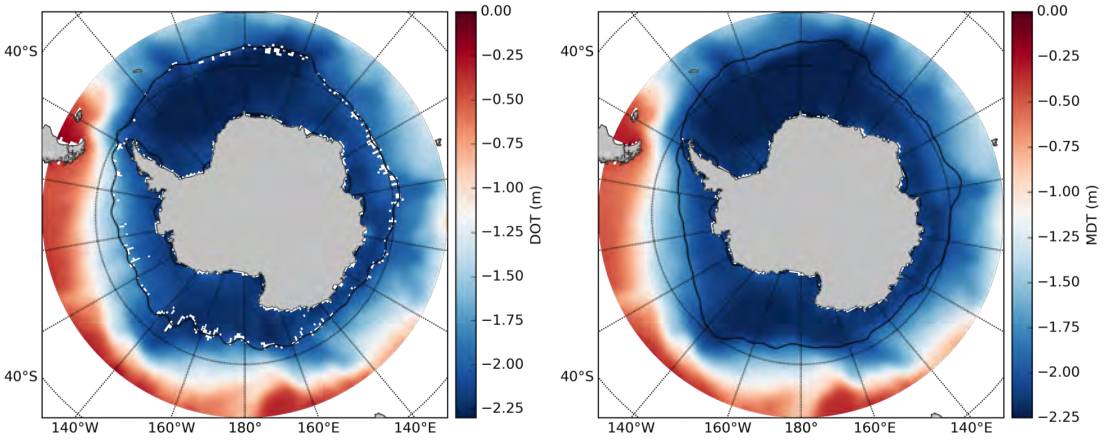

Figure 12: Gridded dynamic ocean topography for September 2015 (left) and mean dynamic topography for 2011 – 2016 (right). Black line corresponds to the 20% sea ice concentration contour.

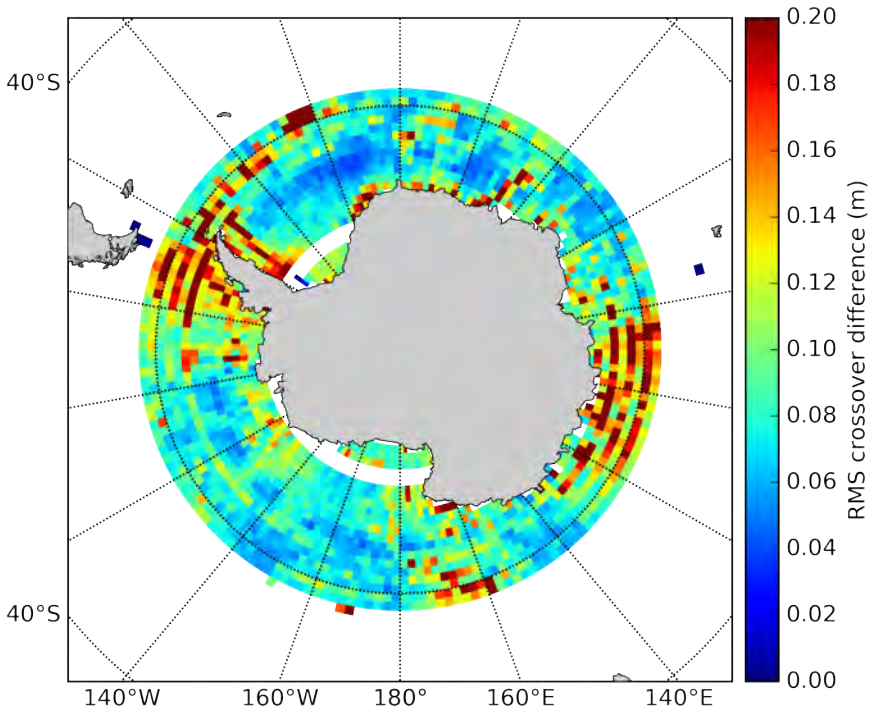

Figure 13: The mean RMS sea surface height difference at crossover locations separated in time by 10 days or less for 2011 – 2016.

tainty contributions for a single sea surface height point, rather than attempting to quantify each one individually. The advantage of this is that each individual source of error can be difficult to calculate, especially in the Southern Ocean, where some corrections rely on poorly-constrained reanalysis or tidal models.

To calculate the RMS difference in sea surface height at crossover locations, the data is binned on a very fine grid, similar in scale to the spatial resolution of the along-track data (approx. 250 m). At orbital crossover locations, the scale of the binning ensures that there are two points per cell, from which the RMS difference is calculated. This is calculated at crossover points where the separation in time is 10 days or less.

Once the RMS difference at crossover locations has been calculated, the data

were gridded onto a regular grid (1° latitude × 2° longitude) and averaged in time to produce a mean RMS crossover difference map (Figure 13). The greatest RMS differences occur in regions of complex bottom topography, namely the Drake Passage region and Indian Sector of the polar Southern Ocean. This is likely to be due increased eddy variability, and the aliasing of these eddies increases the RMS difference in these regions. The mean uncertainty is estimated by dividing by the square root of the number of satellite passes (average 425 per month). This, the standard error of the gridding method, and the standard error of the ocean-ice offset are added in quadrature,

$$\mathrm{Error}_{\mathrm{Ocean}} = \sqrt{\mathrm{Error}_{\mathrm{Crossover}}{}^2 + \mathrm{Error}_{\mathrm{Grid(Ocean)}}{}^2} \tag{6}$$

$$\mathrm{Error}_{\mathrm{Ice}} = \sqrt{\mathrm{Error}_{\mathrm{Crossover}}{}^2 + \mathrm{Error}_{\mathrm{Grid(Ice)}}{}^2 + \mathrm{Error}_{\mathrm{Offset}}{}^2} \tag{7}$$

where $\mathrm{Error}_{\mathrm{Crossover}} = 0.48$ cm is the uncertainty calculated from the orbital crossover locations, $\mathrm{Error}_{\mathrm{Grid(Ocean)}} = 0.28$ cm and $\mathrm{Error}_{\mathrm{Grid(Ice)}} = 0.59$ cm are the standard errors for the gridded product in the ice-free and ice-covered ocean regions, respectively, and $\mathrm{Error}_{\mathrm{Offset}} = 0.29$ cm is the standard error of the ocean–ice offset added to the lead-derived altimetry data. These calculations give a monthly uncertainty of 0.56 cm for the ice-free ocean, and 0.81 cm for the ice-covered ocean.

3.5.1 Satellite sampling pattern

The spatial variation of the sea surface height anomaly has a smaller amplitude within the sea ice region than in the ice free ocean (Figure 14). This low amplitude

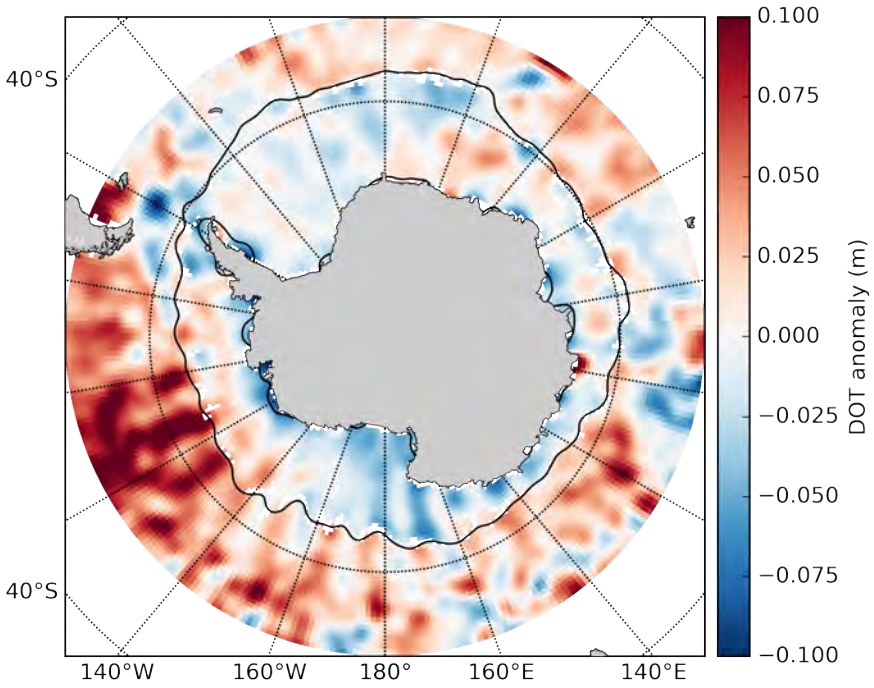

Figure 14: Dynamic ocean topography anomaly for September 2015. Black line indicates the 20% sea ice concentration contour.

region reveals a meridional striping pattern, which is especially visible in the Ross Sea. These patterns likely arise due to the fact that the satellite does not measure the entire Southern Ocean at once, but collects data over the course of a single month (Figure 15). Ocean dynamics occurring on timescales shorter than a month cause the sea surface height to change and so the last satellite pass in a month will not measure the same sea surface height as the first, resulting in this aliasing effect. This is amplified in the sea ice region because the distance between adjacent satellite tracks decreases the closer they get to the pole. These patterns are also visible in the correlation maps in Section 3.6.

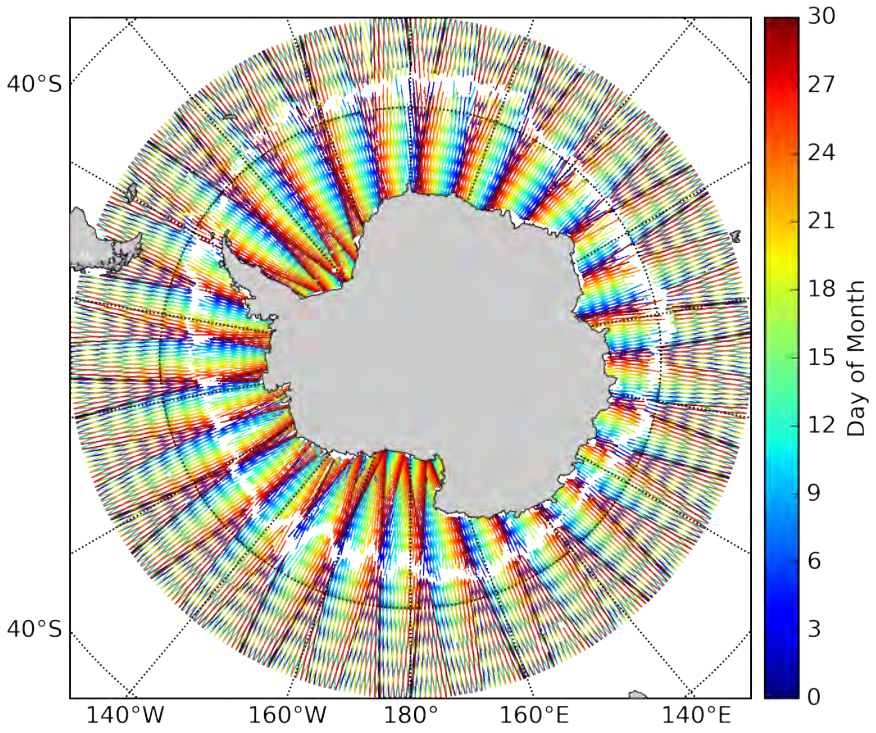

Figure 15: Along-track points for September 2015, colours correspond to the day of the month on which the measurement was taken.

3.6 Validation of Dataset

In order to assess whether the CryoSat-2 data reasonably captures the sea surface height variability in the polar Southern Ocean, the data were correlated with the SAM index and *in situ* bottom pressure recorders. Coastal tide gauges were also considered for this, however the tide gauges that were available did not have a sufficient data overlap with the CryoSat-2 dataset making them inadequate for validating the CryoSat-2 dataset. The resulting correlation maps (Figures 16 and 17) show spatial patterns that mirror the sea surface height response that is expected from variations measured in either the SAM index or bottom pressure recorders.

3.6.1 SAM index

The strength of the westerlies in the Southern Ocean and the subsequent wind stress is an important driver of equatorward Ekman transport, and therefore the SAM has a negative correlation with the sea level (Figure 16). Positive/negative SAM means stronger/weaker westerlies, which enhance/reduce the northward Ekman transport and result in a lower/higher sea surface height around the continent.

The correlation pattern in Figure 16 leads to the conclusion that the sea surface height measurements by CryoSat-2 reasonably capture the seasonal-to-annual variability of the SAM. The physical drivers behind the relationship between the wind pattterns of the Southern Ocean, the northward/southward Ekman transport, and the fall/rise of the sea surface height around the Antarctic Continent readily explain this pattern (Hughes et al., 1999, 2003).

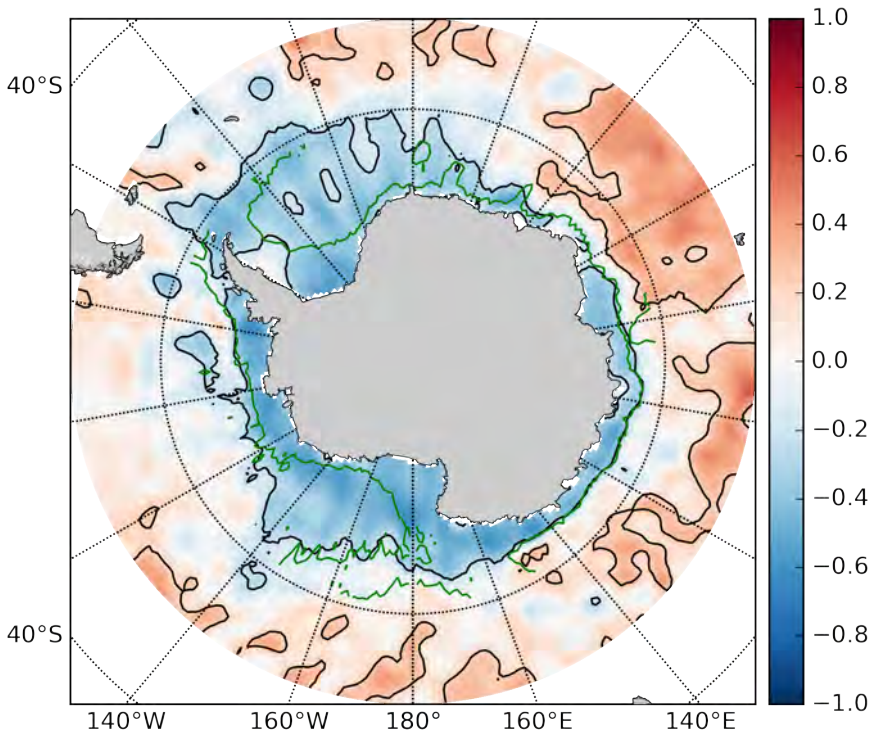

Figure 16: Correlation map of SAM index and sea surface height anomaly data. Black contours correspond to p = 0.2. Green contours are the 3500 m depth contour (> 60°S only).

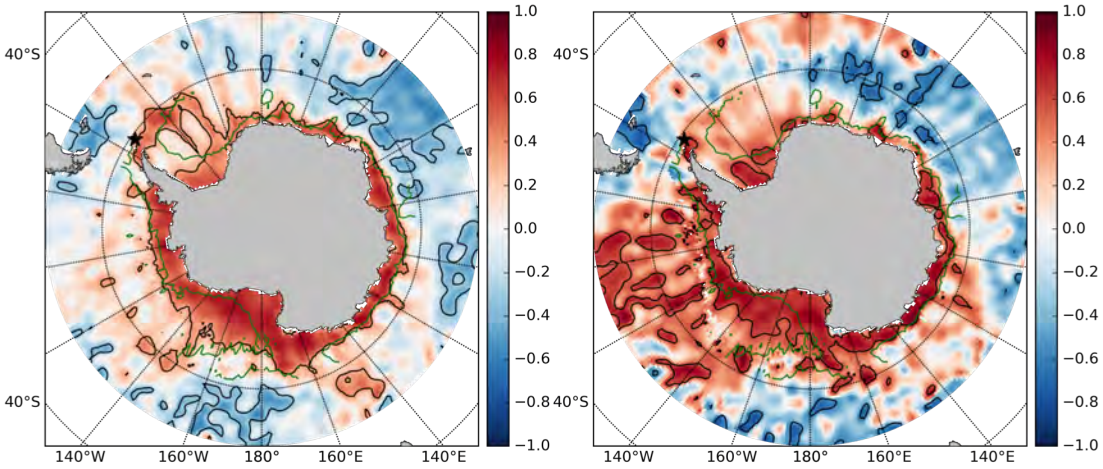

Figure 17: Correlation maps of Drake Passage South Deep (left) and Drake Passage South (right) bottom pressure recorder data with sea surface height anomaly data. Black contours correspond to p = 0.2. Black stars show the location of the BPRs. Green contours are the 3500 m depth contour (> 60°S only).

3.6.2 *In situ* bottom pressure recorders

The correlation between the CryoSat-2 altimetry data and *in situ* bottom pressure recorders produce correlation maps (Figure 17) that show positive correlation with altimetry in a pattern that corresponds well with the 'Southern Mode' (Hughes et al., 2003, 1999). The correlation pattern from 'Drake Passage South' recorder (Figure 17, right) shows higher correlations in the Pacific sector of the Southern Ocean than that of the 'Drake Passage South Deep' recorder. This is likely due to variability upstream of the Antarctic Circumpolar Current being transferred to the recorder along streamlines, and 'Drake Passage South' is more sensitive to this because it is located at a shallower depth than 'Drake Passage South Deep'. The fact that 'Drake Passage South Deep has a longer overlap with the CryoSat-2 data would also contribute to a better correlation pattern.

The correlation map produced by a bottom pressure recorder on the north side

of the Antarctic Circumpolar Current axis does not produce such a pattern, due to being outside the f/H contours within which the 'Southern Mode' is bound. The southern correlation maps indicate that the altimetry dataset captures the circumpolar coherence of the 'Southern Mode' and therefore is a reasonable measure of the regional variability of the Antarctic continental shelf.

These correlations were repeated using altimetry with the 'constant' offset applied (Section 3.2.2), and although the correlation patterns were similar, the strength was significantly lower, reinforcing the justification that the 'seasonal' offset is best.

3.7 Discussion

In this section, the ability of the CryoSat-2 data to reasonably capture the large scale variability of the polar southern ocean is assessed. Initial along-track processing performed on the data is similar to that of work done using the same data in the Arctic (Tilling et al., 2017; Armitage et al., 2016), however with some small differences such as the use of a combined geoid model to calculate dynamic ocean topography and calculating the retracker offsets using along-track data. Calculation of the errors and uncertainty results in values that are similar to those previous studies. The use of similar techniques and calculation of uncertainties supports the idea that this data is of comparable quality to that of the Arctic.

Validation of this dataset with the SAM index and *in situ* bottom pressure recorders shows a coherent 'halo' around the continent that is bounded by the continental shelf break (Figures 16, 17). This pattern is consistent with the 'Southern Mode', a coherent halo of variability in sea surface height and pressure on the

continental shelf around Antarctica (Hughes et al., 1999). Hughes et al. (2003) showed that these variations are driven by Southern Annular Mode variability using tide gauges and bottom pressure gauges and follow f/H contours along the Antarctic continental shelf. As with the 'Southern Mode', the correlation 'halo' observed in Figure 16 extends away from the shelf break in the Ross and Weddell Gyre regions. This implies that the coherence observed on the continental shelf that is attributed with the 'Southern Mode' also exists within the gyre systems.

3.8 Conclusion

In conclusion, the results of these processing and analysis steps show that the CryoSat-2 provides an altimetry dataset that is of similar quality to that used in the Arctic (Tilling et al., 2017; Armitage et al., 2016) and that it reasonably captures the monthly variability in the region when compared to independent datasets such as the Southern Annular Mode climate index, and *in situ* bottom pressure recorders. The observed patterns correspond well with the coherent circumpolar variability of the 'Southern Mode' (Hughes et al., 2003), and show that for the purposes of this study, to investigate the seasonal variability of the polar Southern Ocean, the efficiency of the dataset is proven.

4 Objective 2: Variability and Drivers of the Antarctic Slope Front System

The Antarctic Slope Front is a prominent dynamic feature on the continental slope around much of Antarctica. Is associated with steeply sloping isopycnals across the shelf break and westward flow that follows the continental slope. It is an important mechanism for regulating the exchange of water masses between the waters of the continental slope and open ocean and as such has been connected to the mass loss of ice shelves and deep water formation (Jenkins et al., 2016; Stewart and Thompson, 2013, 2012; Mathiot et al., 2011; Chavanne et al., 2010; Baines, 2009). Understanding of the variability of the Antarctic Slope Front is vital if the impact of these processes is to be quantified with greater accuracy.

In this section, the variability of the Antarctic Slope Front is investigated using the novel dataset of sea surface height measurements in the sea ice zone. The dataset's ability to measure the ocean throughout the season provides a novel view of the Antarctic Slope Front, and allows its seasonal variation to be observed. First, in Section 4.1 the Antarctic Slope Font signature in the sea surface height and dynamic ocean topography data products is analysed and the spatial and temporal patterns of the seasonal cycle are calculated. In Section 4.2 the drivers of the seasonal variability are investigated using a composite dataset of ocean surface stress and Maximum Covariance Analysis.

4.1 Detection of Seasonal Variability in the Antarctic Slope Front

The signature of the Antarctic Slope Front is detectable in the sea surface height data and is characterised by a slope upward towards the Antarctic coast (Figure 18). Here, data between 0°E – 90°W were zonally averaged and the meridional distance was measured away from the Antarctic coastline in order to preserve zonal coherence near the coastline. The signature of the Antarctic Slope Front is defined here with a negative (off-coast) meridional gradient in the dynamic ocean topography within 300 km of the coastline (Figure 18). The mean gradient of the dynamic ocean topography data < 300 km from the Antarctic coastline was taken, and monthly zonal averages show seasonal changes (Figure 19).

The gradient is negative, and the associated flow westward, throughout the year (Figure 18). The maximum gradient occurs during the months April – June, while the minimum occurring during December – February. The westward current is maximum in late autumn, and minimum in summer. These two extremes are highlighted in Figure 18, which shows that during April – June the meridional gradient close (< 300km) to the coastline is steeper than in December – February. The gradient of the slope further (> 300 km) from the coast does not change between these two seasonal periods (Figure 18), implying that the current acceleration is limited to the continental slope.

Figures 18 and 19 highlight the seasonality of the zonal-mean Antarctic Slope Front and show that there is an increase in the dynamic ocean topography slope near the Antarctic coastline in autumn. However, it is unclear from these figures alone whether this seasonal change is ubiquitous along the Antarctic coastline or

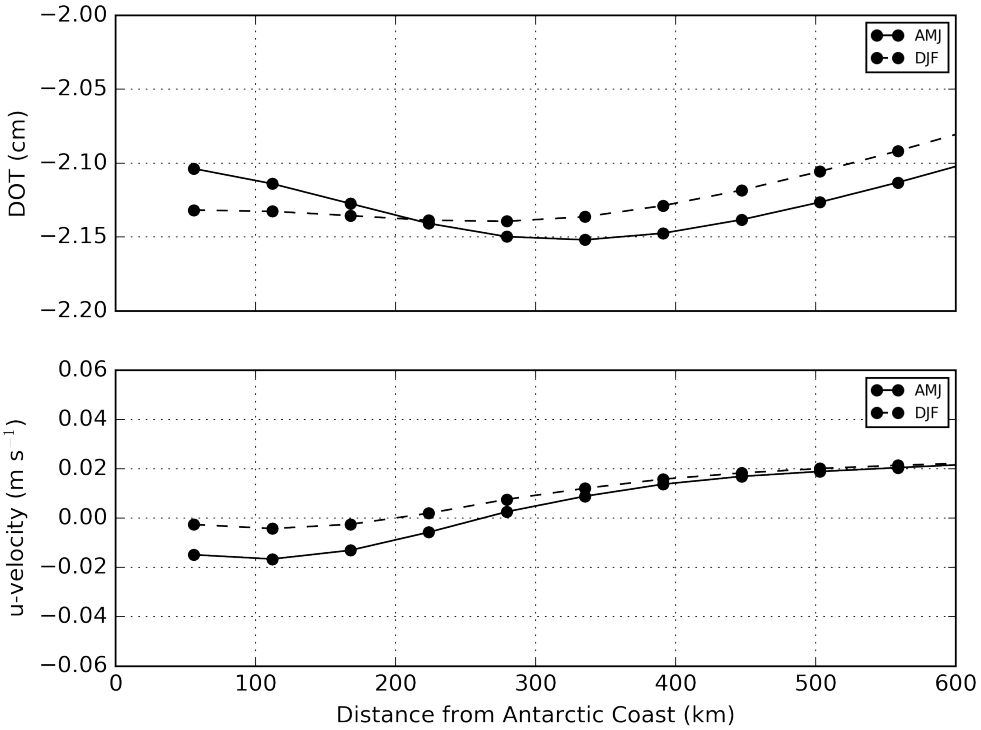

Figure 18: Zonally averaged mean dynamic ocean topography (top) and calculated geostrophic flow (bottom). April – June (solid line) and December – February (dashed line).

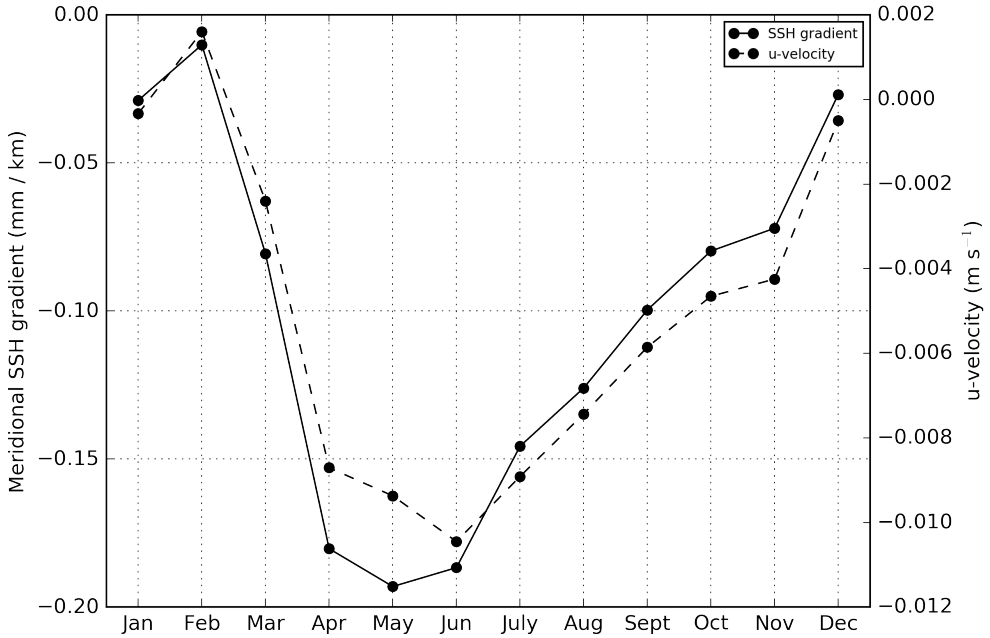

Figure 19: Monthly average meridional mean dynamic topography gradient (solid line) and u-velocity (dashed line) within 300 km of the Antarctic coastline.

only present in small, but mean-dominant, regions. To discover the extent along the Antarctic coastline, the meridional gradient is taken for each month. All April – June and December – February periods are averaged and then subtracted from each other, producing an anomaly map (Figure 20, left). This shows that close to the coastline, nearly all the gradient anomaly is negative, indicating that the slope near the coastline gets steeper in April – June when compared to December – February.

The greatest increase in meridional slope occurs along the coastline in the Indian region of the Polar Southern Ocean, while smaller increases occur in the Ross and Weddell Seas along the edge of the continental shelf (Figure 20). The reason for the strongest signal in the Indian sector is not immediately clear, as the meridional gradient of a uniform off-coast slope will show the strongest signal

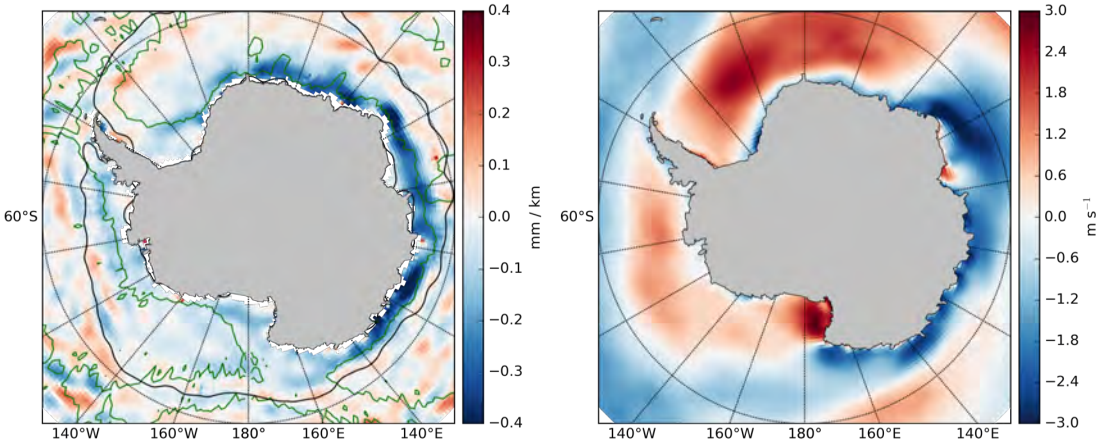

Figure 20: Left: Meridional gradient anomaly between April – June and December – February. Black line is the average September 10% sea ice concentration contour. Green line is the 3500 m depth contour. Right: 10 m u-wind anomaly for the same period.

in regions where the coast is zonal (i.e the coastline in the Indian sector). So to investigate this, the same April – June minus December – February anomaly is calculated for the 10 m zonal wind component from ERA Interim reanalysis (Dee et al., 2011). This shows that the zonal wind component anomaly close to the Antarctic coast is strongest (and negative) in the Indian sector (Figure 20, right) indicating a strengthening of easterly winds near the coastline which would act to enhance the coastward Ekman transport, increasing the sea level slope near the coast.

4.2 Investigating the Drivers of Seasonal Variability in Antarctic Slope Front

It has been established that the gradient of the meridional slope close to the coast is maximum in autumn and minimal in summer (Figure 19) and that an increase

in zonal flow can be attributed to changes in the wind field (Figure 20). In this region, a direct comparison between the altimetry and the wind field alone does not provide an accurate representation of their relationship, as the wind stress on the ocean is heavily influenced by the presence of sea ice. Instead, the wind stress, sea ice concentration, and sea ice drift data are combined into an ocean surface stress and the links between it and altimetry are investigated.

4.2.1 Ocean Surface Stress

Sea ice acts to damp the effect of wind stress on the ocean, though it does not diminish it entirely. When investigating the effect of wind stress on the ocean in sea ice regions, the wind stress on the ice floes needs to be accounted for, as the resulting stress of the ice drift on the ocean is non-zero. A composite dataset is presented here, using wind stress, sea ice concentration, and sea ice drift data.

In regions where sea ice is present, the wind stress is converted into ocean surface stress using the following equations:

$$\vec{\tau} = \alpha\vec{\tau}_{ice-water} + (1-\alpha)\vec{\tau}_{air-water} \tag{8}$$

where

$$\vec{\tau}_{ice-water} = \rho_{water} C_{iw} |\vec{U}_{ice}| \vec{U}_{ice}, \tag{9}$$

$$\vec{\tau}_{air-water} = \rho_{air} C_{d} |\vec{U}_{air}| \vec{U}_{air}, \tag{10}$$

α is sea ice concentration, ρ_{air} is 1.25 kg/m^3, ρ_{water} is 1028 kg/m^3, C_d and C_{iw}

are the air-water and ice-water drag coefficients (1.25×10^{-3} and 5.50×10^{-3} respectively, (Tsamados et al., 2014)). C_{iw} is considered constant as sensitivity tests showed that results were qualitatively independent of C_{iw} (S. Dotto et al., 2018). The curl of the ocean surface stress was then taken and its relationship with the altimetry was investigated using Maximum Covariance Analysis.

4.2.2 Maximum Covariance Analysis

Maximum Covariance Analysis (MCA) shows spatiotemporal patterns of covariability between two datasets by taking the Single Value Decomposition of their covariance matrix (Wallace et al., 1992). This was performed on the data falling between 2011 – 2015, due to the time limitations of both the altimetry data (2011 – 2016) and the ocean surface stress data (limited by the sea ice drift data, 2011 – 2015) for the entire altimetry domain ($> 50°$S, -180 – $180°$E). Both the altimetry and ocean surface stress data had their linear trends and means removed. This analysis was also performed on the dynamic ocean topography meridional gradient rather than the sea surface height anomaly in order to investigate the role of the ocean surface stress on the sea surface slope, and therefore the zonal currents, associated with the Antarctic Slope Front.

The results of Maximum Covariance Analysis are shown in Figures 21 and 22. The first mode, MCA(1), explains 45% of the covariance between the sea surface height anomaly and the ocean surface stress curl, while the second MCA(2) explains 20%. When the sea surface height anomaly is substituted for the meridional gradient of the dynamic ocean topography, MCA(1) explains over 80% of the covariance, while MCA(2) explains 5%. The Principal Components (PC) for each Maximum Covariance Analysis mode are shown in Figure 22 (top and bot-

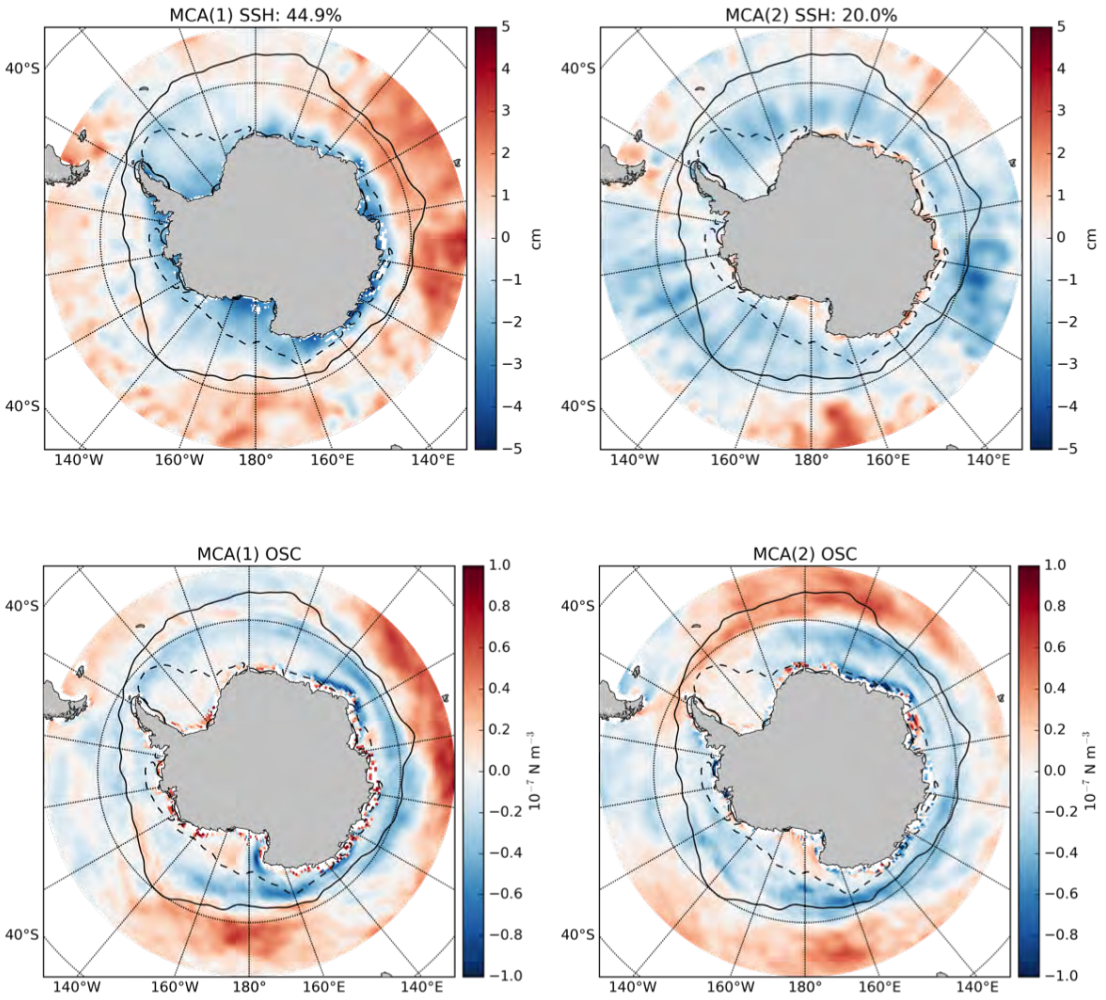

Figure 21: The first (left) and second (right) Maximum Covariance Analysis modes contributing to the altimetry sea surface height (top) and ocean surface stress curl (bottom). Black lines are the average 10% sea ice concentration contour for September (solid) and March (dashed).

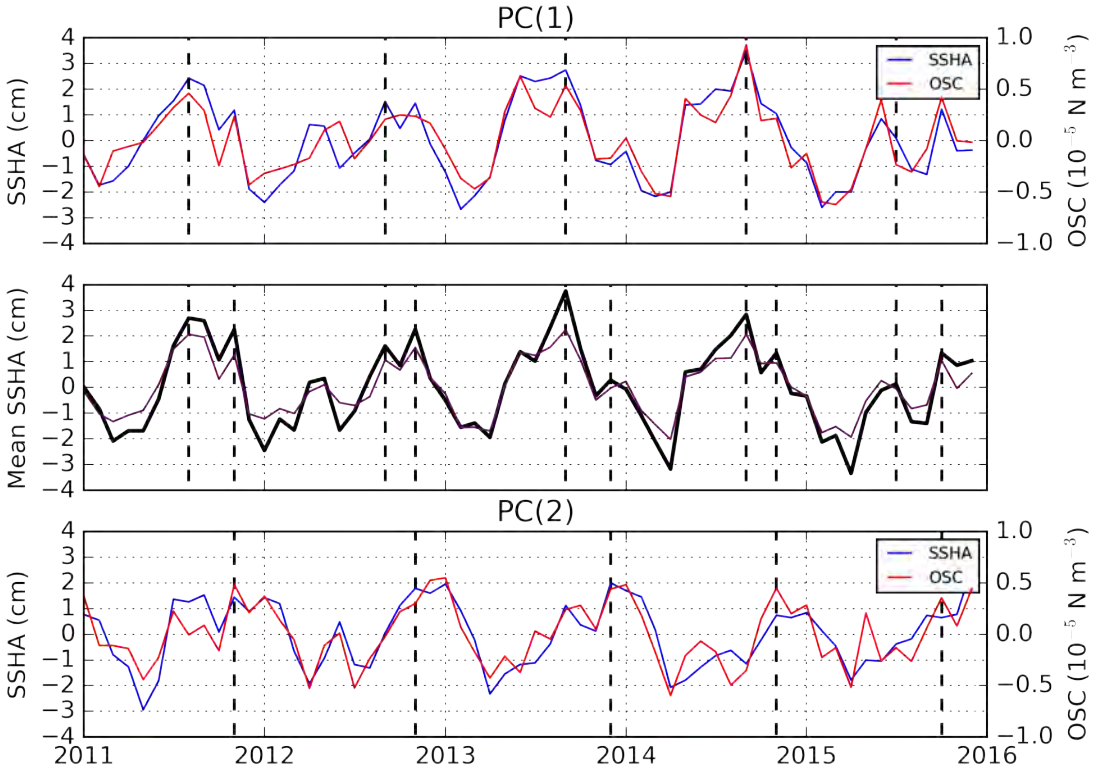

Figure 22: The principal components of the first (top) and second (bottom) Maximum Covariance Analysis modes and the mean sea surface height anomaly within the Polar Southern Ocean (thick black line, centre). Blue/red lines (top, bottom) are principal components for the sea surface height/ocean surface stress modes. Purple line (centre) is the sea surface height anomaly calculated from the weighted mean of the two blue lines. Vertical dashed lines highlight the two peaks in the seasonal cycle of the sea surface height anomaly.

tom panes). The correlation coefficient between each principal component and the SAM index is calculated. This produces a coefficient of 0.58 ($p < 0.01$) and 0.16 ($p = 0.2$) for the first and second sea surface height modes, and 0.57 ($p < 0.01$) and 0.28 ($p = 0.02$) for the ocean stress curl modes.

The results from the spatial (Figure 21) and temporal (Figure 22) patterns, combined with the correlation coefficients with SAM point towards both the first and second sea surface height modes being driven primarily by variations in the

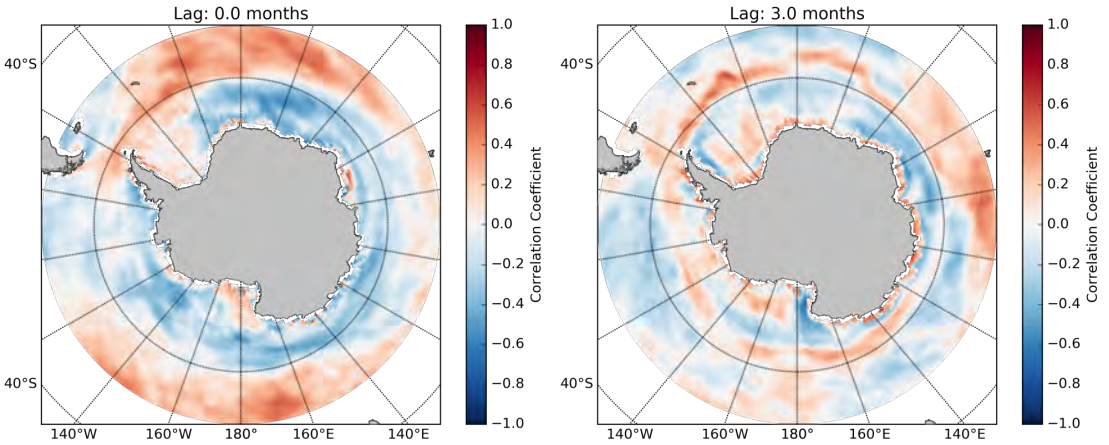

Figure 23: Lagged (0 months, left; 3 months, right) correlation maps between the gridded ocean surface stress curl and sea surface height PC(2).

surface stress, with MCA(2) having a lower sensitivity. Spatial patterns in the ocean surface stress curl (Figure 21, bottom) both show similar, annular patterns with little zonal variation between modes while the sea surface height modes (Figure 21, top) are significantly different.

To further investigate the lead-lag relationship between the wind field (the dominant element in the ocean surface stress) and the principal components, cross correlation analysis was performed between each principal component and the SAM index. The highest correlation between the SAM index and PC(1) was found to be 0.57 ($p < 0.01$) at zero lag, while the highest correlation with PC(2) was 0.23 ($p < 0.01$) with a lag of 3 – 4 months. Furthermore, calculating the cross correlation between PC(1) and PC(2) for the sea surface height resulted in a maximum correlation of 0.56 ($p < 0.01$), also with a lag of 3 – 4 months.

Maximum Covariance Analysis only calculates covariance modes at zero lag, so cross-correlation analysis was employed to investigate lead-lag relationships between the ocean surface stress curl and the sea surface height. Figure 23 shows

lagged correlation maps between the sea surface height PC(2) and the gridded ocean surface stress curl data. The zero-lag correlation pattern (right panel) matches the MCA(2) ocean surface stress curl pattern in Figure 21 (bottom right panel). The correlation map at 3 months lag (when the ocean surface stress curl leads the sea surface height) in the right panel shows a similar pattern (mostly blue within much of the polar Southern Ocean) to that of the MCA(2) sea surface height pattern in Figure 21 (top right panel), albeit with a ring of positive correlation along the edge of the sea ice at maximum extent.

Initial discovery of this ring lead to the hypothesis that this pattern was caused by increased sea ice drift at the sea ice edge as it approaches the southernmost boundary of the Antarctic Circumpolar Current in winter. However, sensitivity tests show that this is not the case. Both setting the sea ice drift to a constant value and removing it entirely from the ocean surface stress curl equation fails to remove this ring pattern in the correlation map. Furthermore, this ring is not present when sea ice is set constant or removed and the sea surface height PC(2) is correlated with just the wind stress. This leads to the conclusion that this ring pattern is a consequence of the parameterisation of sea ice in the ocean surface stress equation. Therefore, for the purposes of this study, it is ignored when interpreting the correlation pattern in Figure 23 (right).

In order to better evaluate the impact of the ocean surface stress on the sea surface height, a timeseries of the polar Southern Ocean sea surface height was calculated. This was defined by taking the weighted mean of the two sea surface height Maximum Covariance Analysis modes (Figure 21, top) and masking out all data outside of the strong (blue) signal within the polar Southern Ocean. This mask was applied to the monthly sea surface height anomaly data and each month

was averaged, producing a timeseries (Figure 22, black solid line). Variations in the mean sea surface height anomaly (black solid line) and the combined results from the two sea surface height principal components (purple solid line) reveal that much of the sea surface height variability is explained by the first two principal components. The small differences between the actual and the reconstructed signals will originate either from outside of the polar Southern Ocean (the principal components are calculated using the whole Southern Ocean domain) or from other modes not shown here (PC(3), etc).

The lagged correlation between the sea surface height principal components and the SAM index lead to the conclusion that PC(2) is a delayed response (with a lag time of 3 – 4 months) to variations in the wind field. This is visible in Figure 22. The seasonal cycle maximum in the mean sea surface height anomaly has a double peak for the majority of the years, which are indicated by the black, vertical, dashed lines. The first peak corresponds to the 'fast' response of the sea surface height to changes in the ocean surface stress curl (MCA(1) and PC(1)), while 3 – 4 months later a second 'delayed response' peak occurs (MCA(2) and PC(2)). The first 'fast' peak in the mean sea surface height anomaly corresponds with a peak in the PC(1), but rarely in PC(2), while the second 'delayed' peak in the mean sea surface height anomaly corresponds with a maximum peak in PC(2), but rarely in PC(1).

4.3 Discussion

The signature of the Antarctic Slope Front is clearly visible in the altimetry data (Figure 18) and displays a prominent seasonal cycle (Figure 19). The seasonal

maximum occurs in April – June while a minimum occurs in December – February, this is the same as in studies that have used *in situ* (Peña-Molino et al., 2016; Núñez-Riboni and Fahrbach, 2009), modelled (Mathiot et al., 2011), and altimetry-derived (Armitage et al., 2018) measurements.

Rough calculation of the average geostrophic transport within 300 km of the Antarctic coast gives a maximum eastward transport of ≈ 8 Sv [10^6 m^3 s^{-1}] which is less than half the mean transport (19.2 Sv) measured by Peña-Molino et al. (2016). Reasons for this difference arise due to the use of altimetry here compared to *in situ* measurements used by Peña-Molino et al. (2016). The currents of the Antarctic Slope Front have been shown to not be entirely barotropic (Peña-Molino et al., 2016; Núñez-Riboni and Fahrbach, 2009) and, as altimetry can only detect the barotropic signal, this underestimation of the transport is expected. Errors near the coast in the geoid model could also contribute to this difference (Section 2.3.2), as the permanent coastal features (Figure 6) could bias the dynamic topography high/low and cause an over/underestimation of the mean transport.

Figure 20 (left) provides a picture of the extent of the April – June maximum in the Antarctic Slope Front, showing that some increase in the meridional gradient is present around much of the Antarctic coast. The strongest increase is clearly in the Indian Sector, and a similar April – June anomaly is present in reanalysis winds (Figure 20, right), indicating that anomalous easterly winds along f/H contours are a contributing element in this (Thompson et al., 2014; Mathiot et al., 2011).

Results from the Maximum Covariance Analysis further supports the finding that wind is a major driver of variability in the Antarctic Slope Front (Figure 21). Combining results from Maximum Covariance Analysis and cross correlation analysis (between the altimetry data, ocean surface stress, and the SAM index) it

is revealed that the sea surface height has a 'fast' and 'slow' response to variations in the wind field. The spatial pattern of the 'fast' response (Figure 21, top left) matches that of the 'Southern Mode', which acts to propagate the sea surface height anomaly response to wind fluctuations rapidly around Antarctica along f/H contours (Hughes et al., 2003, 1999). The signature of this mode in the sea level is an 'anti-phase' (Armitage et al., 2018) response between the waters on the continental shelf and those of the surrounding deep ocean basins (Figure 21, top right). 3 – 4 months later, the 'slow' response causes a sea level response over the entire Southern Ocean which appears to diminish to zero between the continental slope and the coastline of Antarctica (Figure 21, top right). Lagged correlation maps further confirm this, as the ocean surface stress curl correlation pattern at 3 months lag (Figure 23, right) matches the sea surface height MCA(2) response pattern (Figure 21, top right).

The effect this has on the along-coast velocity is also important, as performing the Maximum Covariance Analysis on the dynamic ocean topography meridional gradient reveals that the 'fast' mode, MCA(1), accounts for over 80% of the covariance, while MCA(2) accounts for just 5%. Both modes appear to alter the sea level on the continental shelf and, by association, the pycnocline depth, however it is MCA(1) that has the greatest influence on the along-slope velocities associated with the Antarctic Slope Front. Furthermore, the Maximum Covariance Analysis patterns reveal that it is not just local surface stress along f/H contours (such as those modelled by Mathiot et al. (2011) and Zika et al. (2013)) that is important for the sea surface height variation on the continental shelf, but rather winds over the whole Southern Ocean.

4.4 Conclusions

In this section, the sea surface height data from CryoSat-2 is combined with other datasets from the Southern Ocean to investigate the seasonal variability and drivers of the Antarctic Slope Front system. This is the first time it has been possible to observe the Antarctic Slope Front system in the large scale and over an entire seasonal cycle as previous studies into this system could only make use of localised *in situ* measurements, or datasets that cover an insufficient time period.

The signature of the Antarctic Slope Front in the sea surface height is observable in the sea surface height data as an upward-sloping gradient towards the Antarctic coastline (Figure 18), and the variation between months throughout the year reveals a prominent seasonal cycle (Figure 19) that coincides with an increase in the meridional slope gradient to a maximum during the months April – June, and a minimum during the months December – February. This seasonal cycle period matches that of other studies using *in situ* measurements of the Antarctic Slope Front in single locations, but also that of modelled and other satellite-based studies. However, the amplitude of the seasonal cycle in geostrophic transport calculated here is notably smaller than that found in *in situ* studies. One likely reason for this is the existence of errors in the geoid model close to the coast that flow into the calculation of the absolute current. Another reason could be that the currents associated with the Antarctic Slope Front are not purely barotropic, and so any inferred currents from altimetry underestimate the associated transport.

Wind and its associated surface stress are revealed to be the most significant driver of sea surface height and transport variations on the Antarctic continental slope. The results of Maximum Covariance Analysis performed on the altimetry

and the ocean surface stress curl, a composite of wind stress, sea ice concentration, and sea ice drift data; reveal that the ocean responds to forcing variation in a two-step process. In response to a change in surface stress across the whole Southern Ocean, the water over the continental shelf rises/falls and the waters of the deep ocean basins surrounding it falls/rises with an antiphase relationship (as observed by Armitage et al. (2018)). The response over the continental shelf is quickly propagated around Antarctica following f/H contours as part of the 'Southern Mode' (Hughes et al., 2003, 1999). 3 – 4 months later, the 'slow' response becomes established, which acts to raise/lower the sea level across the entire Southern Ocean basin ($> 50°$S). This is visible in the 'double peak' in mean sea surface height shown in Figure 22 (middle panel). When combined, these two modes explain the vast majority of the Polar Southern Ocean variability and the 'fast' mode explains over 80% of the zonal transport variability on the continental slope.

Finally, the presence of sea ice in the surface stress equation has a vitally important role in regulating the influence of wind stress on the ocean. If sea ice were not present, even small wind stress variations would have a much greater impact on the ocean than what is observed in reality. Furthermore, the addition of sea ice drift prolongs the effect of wind, as drifting sea ice preserves momentum and so the effects of wind stress are increased in duration thanks to moving sea ice. Studies looking at the interactions between the ocean and the atmosphere in regions where sea ice is prevalent should take account of this.

5 Summary and Conclusions

This study uses a uniquely processed satellite altimetry dataset to analyse the seasonal-to-interannual variability of sea surface height within the polar Southern Ocean. The novel retracking algorithm developed at the Centre for Polar Observation and Modelling, UCL, enables sea surface height measurements to be taken within the sea ice zone by the ESA satellite CryoSat-2 (Tilling et al., 2017, and references therein). This provides the ability to observe ocean dynamics in the polar Southern Ocean throughout a full seasonal cycle where sea ice growth and retreat previously made such large-scale observations impossible. Here, the UCL-retracked CryoSat-2 dataset is used in combination with other datasets such as climate indices, *in situ* bottom pressure recorders, sea ice concentration and ice drift products to analyse and assess the variability of the polar Southern Ocean and its driving mechanisms.

The first objective of this study was to assess whether the CryoSat-2 dataset was able to capture the variability of sea surface height in the polar Southern Ocean. This was completed by first processing the raw altimetry measurements and manipulating them into a useable product. The data was filtered and compared to standard altimetry products before a geoid model was used to convert the sea surface height measurements into dynamic ocean topography. A major step in this was to calculate and correct for an 'offset' that occurred in the data along boundaries between the open ocean and sea ice. It is likely that this offset occurs due to differences in the retracking algorithms for the open ocean and sea ice leads, though another possibility is the presence of melt ponds on top of sea ice floes which have a similar return to leads and because of sea ice freeboard this

biases the sea surface height measurement high. A great method for determining the source of this offset would be to process the entire dataset using the lead retracker, thus removing processing differences across the boundary.

The data was then interpolated onto a regular monthly grid, which enabled a mean dynamic ocean topography to be calculated, from which monthly anomalies were taken. This allowed the dataset to be compared against other data products and enabled time series analysis. To confirm that the dataset reasonably captured the dynamic variability of the polar Southern Ocean, the correlation between altimetry, SAM index, and *in situ* bottom pressure recorders was calculated. The resulting correlation map showed patterns that were a good match for the expected dynamical response of the polar Southern Ocean to variations in the SAM index and *in situ* bottom pressure recorders. Because of this, it is concluded that the CryoSat-2 dataset has the ability to capture the dynamic variability of the ocean in the presence of sea ice.

The second objective was to identify and analyse the variability of the Antarctic Slope Front system and asses its dominant driving mechanisms. The signature of the Antarctic Slope Front is clearly visible in the data as a slope in dynamic ocean topography upwards towards Antarctic coastline. From a zonal mean perspective, this upward slope extends to about 300 km from the coast, and its gradient is maximum at the start of winter (April – June) and minimal in summer (December – February). This increase in off-coast slope is ubiquitous around the Antarctic continent, but is strongest in the Indian sector and it is shown that an increase in zonal winds during the April – June period is the likely cause for this.

The importance of wind forcing in the polar Southern Ocean is stressed, and its influence on the continental shelf is shown here. A composite of wind stress,

sea ice concentration, and sea ice drift data is used here to parameterise the ocean surface stress in sea ice regions and investigate the effects of wind stress on the continental shelf sea surface height. Maximum Covariance Analysis and cross correlation analysis was used to show that surface stress over the Southern Ocean drives a two step response in the sea surface height. Changes in surface stress initially cause an antiphase response in the sea surface height between the waters on and off the continental shelf. On the shelf, the response is propagated around the continent, bounded by f/H contours, rapidly. This mechanism means that even local winds can cause a circumpolar response in sea level. It is this rapid response that alters the off-coast sea level slope, and so would cause changes to the Antarctic Slope Front and the pycnocline depth. 3 – 4 months later, the delayed response acts to raise/lower the sea level across the whole Southern Ocean, a response that diminishes on the continental shelf and is zero at the coastline. This delayed response does not make significant changes to the Antarctic Slope Front, and it is hypothesised that it also does not affect the pycnocline depth.

From these observations, it is clear that the Antarctic Slope Front is driven primarily by variations in ocean surface stress. Variations in wind forcing are felt immediately on the continental shelf and the changes to the off-coast sea surface slope will alter the circumpolar transport by the frontal system. It is hypothesised that these mechanisms will also change the depth of the pycnocline. Therefore this has the ability to change the on-shelf water properties, thus affecting climatologically important processes such as Antarctic Bottom Water formation and ice shelf mass loss. This study can be further developed by incorporating *in situ* hydrographic profiles of shelf waters throughout the seasonal cycle. Doing so will provide a sub-surface perspective on the changes that may occur in response

to the forcing variations observed in this study and shed further light on how the Antarctic Slope Front system and shelf water properties are affected. Also, sea surface height data from CryoSat-2 and other satellites whose data can be processed using the UCL lead retracker could be assimilated into an under-ice circulation model, to better understand the response of large scale overturning to variations in climate forcing.

References

T. W. K. Armitage, S. Bacon, and A. L. Ridout. Arctic sea surface height variability and change from satellite radar altimetry and GRACE, 2003–2014. *Journal of Geophysical Research: Oceans*, 2016.

T. W. K. Armitage, R. Kwok, A. F. Thompson, and G. Cunningham. Dynamic topography and sea level anomalies of the Southern Ocean: Variability and teleconnections. *Journal of Geophysical Research: Oceans*, 123(1):613–630, 2018.

P. G. Baines. A model for the structure of the Antarctic Slope Front. *Deep Sea Research II*, 2009.

C. W. Böning, A. Dispert, M. Visbeck, S. R. Rintoul, and F. U. Schwarzkopf. The response of the Antarctic Circumpolar Current to recent climate change. *Nature Geoscience*, 1(12):864–869, 2008.

C. Bouzinac. CryoSat product handbook. *ESA User Manual, ESA, ESRIN, Italy*, 4121:4123, 2014.

A. I. Bulczak, S. Bacon, A. C. Naveira Garabato, A. Ridout, M. J. P. Sonnewald, and S. W. Laxon. Seasonal variability of sea surface height in the coastal waters and deep basins of the Nordic Seas. *Geophysical Research Letters*, 42(1):113–120, 2015.

D. J. Cavalieri, C. L. Parkinson, P. Gloersen, and H. J. Zwally. Sea ice concentrations from nimbus-7 smmr and dmsp ssm/i-ssmis passive microwave data [concentration]. *NASA DAAC at the National Snow and Ice Data Center, 1996, updated yearly*, 2012.

C. P. Chavanne, K. J. Heywood, K. W. Nicholls, and I. Fer. Observations of the Antarctic slope undercurrent in the southeastern Weddell Sea. *Geophysical Research Letters*, 37(13), 2010.

D. P. Dee, S. M. Uppala, A. J. Simmons, P. Berrisford, P. Poli, S. Kobayashi, U. Andrae, M. A. Balmaseda, G. Balsamo, P. Bauer, P. Bechtold, A. C. M. Beljaars, L. van de Berg, J. Bidlot, N. Bormann, C. Delsol, R. Dragani, M. Fuentes, A. J. Geer, L. Haimberger, S. B. Healy, H. Hersbach, E. V. Hólm, L. Isaksen, P. Kållberg, M. Köhler, M. Matricardi, A. P. McNally, B. M. Monge-Sanz, J.-J. Morcrette, B.-K. Park, C. Peubey, P. de Rosnay, C. Tavolato, J.-N. Thépaut, and F. Vitart. The ERA-Interim reanalysis: Configuration and performance of the data assimilation system. *Quarterly Journal of the Royal Meteorological Society*, 137(656):553–597, 2011.

M. R. Drinkwater, R. Francis, G. Ratier, and D. J. Wingham. The European Space Agency's earth explorer mission CryoSat: Measuring variability in the cryosphere. *Annals of Glaciology*, 39(1):313–320, 2004.

C. Förste, S. L. Bruinsma, O. Abrikosov, J.-M. Lemoine, J. C. Marty, F. Flechtner, G. Balmino, F. Barthelmes, and R. Biancale. EIGEN-6C4 The latest combined global gravity field model including GOCE data up to degree and order 2190. *Advances in Space Research*, 2014.

C. R. Francis. CryoSat mission and data description. 2007.

K. A. Giles, S. W. Laxon, A. L. Ridout, and D. J. Wingham. Western Arctic Ocean freshwater storage increased by wind-driven spin-up of the Beaufort Gyre. *Nature Geoscience*, 2012.

A. E. Gill. Circulation and bottom water production in the Weddell Sea. In *Deep Sea Research and Oceanographic Abstracts*, number 2 in 20, pages 111–140. Elsevier, 1973.

H. H. Hellmer, F. Kauker, R. Timmermann, J. Determann, and J. Rae. Twenty-first-century warming of a large Antarctic ice-shelf cavity by a redirected coastal current. *Nature*, 485(7397):225, 2012.

C. W. Hughes, M. P. Meredith, and K. J. Heywood. Wind-driven transport fluctuations through Drake Passage: A southern mode. *Journal of Physical Oceanography*, 29(8):1971–1992, 1999. ISSN 0022-3670.

C. W. Hughes, P. L. Woodworth, M. P. Meredith, V. Stepanov, T. Whitworth, and A. R. Pyne. Coherence of Antarctic sea levels, Southern Hemisphere annular mode, and flow through Drake Passage. *Geophysical Research Letters*, 2003.

S. S. Jacobs. On the nature and significance of the Antarctic Slope Front. *Marine Chemistry*, 35:9–24, 1991.

S. S. Jacobs. Bottom water production and its links with the thermohaline circulation. *Antarctic Science*, 2004.

A. Jenkins, P. Dutrieux, S. Jacobs, E. J. Steig, G. H. Gudmundsson, J. Smith, and K. J. Heywood. Decadal ocean forcing and Antarctic ice sheet response: Lessons from the Amundsen Sea. *Oceanography*, 29(4):106–117, 2016.

R. Kwok and J. Morison. Sea surface height and dynamic topography of the ice-covered oceans from CryoSat-2: 2011–2014. *Journal of Geophysical Research: Oceans*, 2015. ISSN 2169-9291.

S. W. Laxon, K. A. Giles, A. L. Ridout, D. J. Wingham, R. Willatt, R. Cullen, R. Kwok, A. Schweiger, J. Zhang, C. Haas, S. Hendricks, R. Krishfield, N. Kurtz, S. Farrell, and M. Davidson. CryoSat-2 estimates of Arctic sea ice thickness and volume. *Geophysical Research Letters*, 40(4):732–737, 2013.

S. Levitus, J. I. Antonov, T. P. Boyer, O. K. Baranova, H. E. Garcia, R. A. Locarnini, A. V. Mishonov, J. R. Reagan, D. Seidov, E. S. Yarosh, and M. M. Zweng. World ocean heat content and thermosteric sea level change (0–2000 m), 1955–2010. *Geophysical Research Letters*, 39(10), 2012.

G. J. Marshall. Trends in the Southern Annular Mode from observations and reanalyses. *Journal of Climate*, 16:4134–4143, 2003.

P. Mathiot, H. Goosse, T. Fichefet, B. Barnier, and H. Gallée. Modelling the seasonal variability of the Antarctic Slope Current. *Ocean Science*, 7(4):445–532, 2011.

T. Mayer-Gürr, R. Pail, T. Gruber, T. Fetcher, M. Rexer, W. D. Schuh, J. Kusche, J. M. Brokmann, D. Rieser, N. Zehentner, A. Kvas, B. Klinger, O. Baur, E. Höck, S. Krauss, and A. Jäggi. The combined satellite gravity field model GOCO05s. 2015.

M. P. Meredith and A. L. Gordon. Synchronous intensification and warming of Antarctic Bottom Water outflow from the Weddell Gyre. *Geophysical Research Letters*, 38, 2011.

M. P. Meredith and A. M. Hogg. Circumpolar response of Southern Ocean eddy activity to a change in the Southern Annular Mode. *Geophysical Research Letters*, 33(16), 2006.

M. P. Meredith, P. L. Woodworth, C. W. Hughes, and V. Stepanov. Changes in the ocean transport through Drake Passage during the 1980s and 1990s, forced by changes in the Southern Annular Mode. *Geophysical Research Letters*, 31 (21), 2004.

I. Núñez-Riboni and E. Fahrbach. Seasonal variability of the Antarctic Coastal Current and its driving mechanisms in the Weddell Sea. *Deep Sea Research Part I: Oceanographic Research Papers*, 56(11):1927–1941, 2009.

A. H. Orsi, G. C. Johnson, and J. L. Bullister. Circulation, mixing, and production of Antarctic Bottom Water. *Progress in Oceanography*, 43(1):55–109, 1999.

N. K. Pavlis, S. A. Holmes, S. C. Kenyon, and J. K. Factor. An Earth Gravitational Model to degree 2160: EGM2008. 2008.

N. R. Peacock and S. W. Laxon. Sea surface height determination in the Arctic Ocean from ERS altimetry. *Journal of Geophysical Research*, 2004.

J. B. Pedro, T. Martin, E. J. Steig, M. Jochum, W. Park, and S. O. Rasmussen. Southern Ocean deep convection as a driver of Antarctic warming events. *Geophysical Research Letters*, 43(5):2192–2199, 2016.

B. Peña-Molino, M. M. S, and S. R. Rintoul. Direct observations of the Antarctic Slope Current transport at 113°E. *Journal of Geophysical Research: Oceans*, 2016.

S. G. Purkey and G. C. Johnson. Warming of global abyssal and deep Southern Ocean waters between the 1990s and 2000s: Contributions to global heat and sea level rise budgets. *Journal of Climate*, 2010.

S. G. Purkey and G. C. Johnson. Antarctic Bottom Water warming and freshening: Contributions to sea level rise, ocean freshwater budgets, and global heat gain. *Journal of Climate*, 2013.

M. Rhein, S. R. Rintoul, S. Aoki, E. Campos, D. Chambers, R. A. Feely, S. Gulev, G. C. Johnson, S. A. Josey, A. Kostianoy, C. Mauritzen, D. Roemmich, L. D. Talley, and F. Wang. Observations: Ocean. In T. F. Stocker, G. Qin, G. K. Plattner, M. Tignor, S. K. Allen, J. Boschung, A. Nauels, Y. Xia, V. Bex, and P. M. Midgley, editors, *Climate Change 2013: The Physical Science Basis. Contribution of Working Group I to the Fifth Assessment Report of the Intergovernmental Panel on Climate Change*. Cambridge University Press, Cambridge, UK and New York, NY, 2013.

S. R. Rintoul. Rapid freshening of Antarctic Bottom Water formed in the Indian and Pacific Oceans. *Geophysical Research Letters*, 2007.

C. D. Rye, A. C. Naveira Garabato, P. R. Holland, M. P. Meredith, G. A. J. Nurser, C. W. Hughes, A. C. Coward, and D. J. Webb. Rapid sea-level rise along the Antarctic margins in response to increased glacial discharge. *Nature Geoscience*, 7(10):732–735, 2014.

T. S. Dotto, A. Naveira-Garabato, S. Bacon, M. Tsamados, P. R. Holland, J. Hooley, E. Frajka-Williams, A. Ridout, and M. J. Meredith. Variability of the Ross Gyre, Southern Ocean: Drivers and responses revealed by satellite altimetry [Accepted]. *Geophysical Research Letters*, 2018.

L. H. Smedsrud, A. Jenkins, D. M. Holland, and O. A. Nøst. Modeling ocean pro-

cesses below Fimbulisen, Antarctica. *Journal of Geophysical Research: Oceans*, 111(C1), 2006.

A. L. Stewart and A. F. Thompson. Sensitivity of the ocean's deep overturning circulation to easterly Antarctic winds. *Geophysical Research Letters*, 39(18), 2012.

A. L. Stewart and A. F. Thompson. Connecting Antarctic cross-slope exchange with Southern Ocean overturning. *Journal of Physical Oceanography*, 43(7): 1453–1471, 2013.

A. F. Thompson, K. J. Heywood, S. Schmidtko, and A. L. Stewart. Eddy transport as a key component of the Antarctic overturning circulation. *Nature Geoscience*, 7(12):879, 2014.

R. L. Tilling, A. Ridout, and A. Shepherd. Estimating Arctic sea ice thickness and volume using CryoSat-2 radar altimeter data. *Advances in Space Research*, 2017.

M. Tsamados, D. L. Feltham, D. Schroeder, D. Flocco, S. L. Farrell, N. Kurtz, S. W. Laxon, and S. Bacon. Impact of variable atmospheric and oceanic form drag on simulations of Arctic sea ice. *Journal of Physical Oceanography*, 44(5): 1329–1353, 2014.

M. C. Tschudi, J. Fowler, J. Maslanik, S. Stewart, and W. Meier. Polar Pathfinder Daily 25 km EASE-Grid Sea Ice Motion Vectors, Version 3. [2010–2016, 50–90S, 140E–70W]. *NASA National Snow and Ice Data Center Distributed Active Archive Center*, 2016.

J. M. Wallace, C. Smith, and C. S. Bretherton. Singular value decomposition of wintertime sea surface temperature and 500-mb height anomalies. *Journal of climate*, 5(6):561–576, 1992.

D. J. Wingham, C. R. Francis, S. Baker, C. Bouzinac, D. Brockley, R. Cullen, P. de Chateau Thierry, S. W. Laxon, U. Mallow, C. Mavrocordatos, L. Phalippou, G. Ratier, L. Rey, F. Rostan, P. Viau, and D. W. Wallis. CryoSat: A mission to determine the fluctuations in Earth's land and marine ice fields. *Advances in Space Research*, 37(4):841–871, 2006. ISSN 0273-1177.

L. Zhang, T. L. Delworth, and F. Zeng. The impact of multidecadal Atlantic meridional overturning circulation variations on the Southern Ocean. *Climate Dynamics*, 2016.

J. D. Zika, J. Le Sommer, C. O. Dufour, A. Naveira-Garabato, and A. Blaker. Acceleration of the Antarctic Circumpolar Current by wind stress along the coast of Antarctica. *Journal of Physical Oceanography*, 43(12):2772–2784, 2013.